Chinese Chemical Letters 37 (2026) 112572

Contents lists available at ScienceDirect

Chinese Chemical Letters

journal homepage: www.elsevier.com/locate/cclet

Solar-driven hydrogen peroxide production on designed g-C_3N_4: Strategies, mechanisms, and perspectives

Zhimin Yuan[a], Xingling Zhao[a], Xianglin Zhu[c,*], Kaili Wang[a], Ya-Qian Lan[b,*], Zaiyong Jiang[a,*]

[a] School of Chemistry & Chemical Engineering and Environmental Engineering, Weifang University, Weifang 261061, China
[b] School of Chemistry, South China Normal University, Guangzhou 510006, China
[c] Institute for Energy Research, Jiangsu University, Zhenjiang 212013, China

ARTICLE INFO

Article history:
Received 13 December 2025
Revised 24 February 2026
Accepted 2 March 2026
Available online 6 March 2026

Keywords:
g-C_3N_4-based photocatalysts
Hydrogen peroxide production
Photocatalytic
Modification strategies
H_2O_2

ABSTRACT

The photocatalytic production of hydrogen peroxide (H_2O_2) utilizing graphitic carbon nitride (g-C_3N_4) offers a sustainable alternative to the conventional, energy-intensive anthraquinone method. Nevertheless, the practical deployment of pristine g-C_3N_4 is constrained by its limited absorption of visible light, rapid recombination of photogenerated charge carriers, and low surface catalytic activity. This review critically examines various modification strategies aimed at enhancing the H_2O_2 generation efficiency of g-C_3N_4-based photocatalysts. Prominent approaches encompass elemental doping, defect modification, and the junction engineering. These modifications synergistically enhance light absorption, facilitate charge separation, and accelerate oxygen reduction reaction kinetics. Consequently, such engineered photocatalysts have achieved H_2O_2 production rates reaching millimolar concentrations per hour under visible-light irradiation, alongside marked improvements in selectivity and apparent quantum efficiency. Despite these significant advancements, challenges persist in realizing broad-spectrum solar energy utilization, ensuring long-term operational stability, and developing scalable synthesis methods for catalyst fabrication. This review delineates prospective research directions aimed at advancing efficient and practical photocatalytic systems for sustainable hydrogen peroxide synthesis.

© 2026 Published by Elsevier B.V. on behalf of Chinese Chemical Society and Institute of Materia Medica, Chinese Academy of Medical Sciences.

1. Introduction

Hydrogen peroxide is recognized as a green oxidant with broad applicability across diverse fields, including wastewater treatment, biomedicine, organic synthesis, chemical sensing, and energy conversion technologies such as fuel cells [1–6]. Its appeal lies in its environmentally benign decomposition pathway, yielding only water and oxygen [7–11]. With the advancement of green chemistry and carbon neutrality goals, H_2O_2 has not only gained prominence as a clean oxidant but is also regarded as a promising energy carrier and electrocatalytic medium within renewable energy systems [12–17]. However, the current industrial production of H_2O_2 predominantly relies on the anthraquinone redox process, which involves organic solvents, anthraquinone carriers, high-pressure hydrogen, and multiple mass-transfer steps [18–20]. This method suffers from complexities in operation, high energy consumption, and significant environmental impact. In response to the demand for green synthesis and decentralized applications, several alternative strategies have been proposed, including the direct synthesis from hydrogen and oxygen, electrocatalytic oxygen reduction, and plasma-assisted processes [21–23]. Nonetheless, these approaches often encounter limitations such as safety concerns, low Faradaic efficiency, or complicated reactor design [24–26]. Hence, there is a pressing need to develop novel H_2O_2 synthesis systems that operate without hazardous gases, under mild conditions, with low energy input, and through clean reaction pathways [27,28].

In recent years, photocatalytic H_2O_2 production has emerged as an attractive alternative, driven by solar energy and utilizing benign reactants such as O_2 and H_2O under ambient conditions [29–32]. In a typical photocatalytic process (Fig. 1a), the photocatalyst absorbs photons with energy equal to or exceeding its band gap, electrons in the valence band are excited to the conduction band, forming electron-hole pairs [33–37]. These unstable pairs then need to separate and migrate to the catalyst's surface,

* Corresponding authors.
E-mail addresses: zhuxl@ujs.edu.cn (X. Zhu), yqlan@m.scnu.edu.cn (Y.-Q. Lan), zaiyongjiang@qlu.edu.cn (Z. Jiang).

https://doi.org/10.1016/j.cclet.2026.112572
1001-8417/© 2026 Published by Elsevier B.V. on behalf of Chinese Chemical Society and Institute of Materia Medica, Chinese Academy of Medical Sciences.

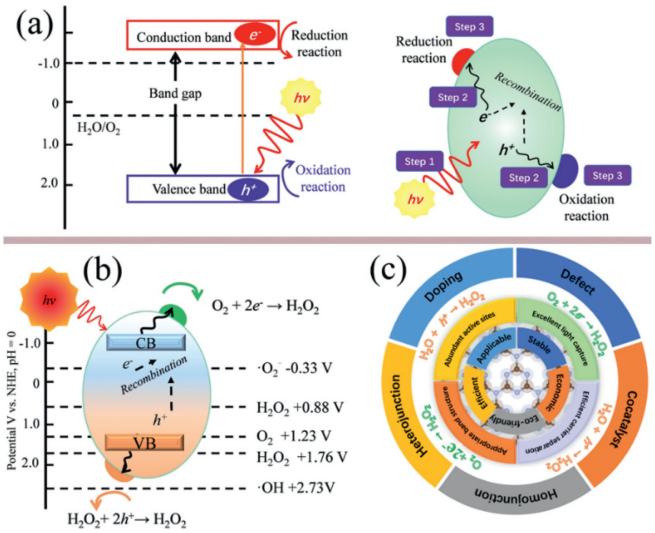


Fig. 1. (a) Schematic diagram of the basic principle of photocatalysis. (b) Photocatalytic preparation of H_2O_2 reaction. (c) The modification strategies schematic of g-C_3N_4.

meaning efficient separation is critical to avoid non-productive recombination that dissipates energy as heat or light. Once on the surface, the electrons react with electron acceptors, while holes oxidize donors; these radical species further drive target redox reactions, with minimizing electron-hole recombination being key to enhancing catalytic efficiency [38–42]. For the H_2O_2 generation, the photoexcited electrons migrate to the conduction band to reduce oxygen molecules into H_2O_2, while the holes can be consumed by sacrificial agents or water oxidation, thereby maintaining charge balance and enabling redox coupling. A critical aspect of this process lies in achieving selective two-electron oxygen reduction (2e⁻ ORR) to form H_2O_2, while avoiding competing pathways such as the four-electron reduction to water or further reduction and decomposition of reactive intermediates.

The photocatalytic synthesis of H_2O_2 can proceed *via* two principal routes: the oxygen reduction reaction (ORR) and the water oxidation reaction (WOR) [43–46]. Upon exposure to light, the photocatalyst generates electron-hole pairs, where the photogenerated electrons drive the reduction of O_2 to H_2O_2, and the photogenerated holes facilitate the oxidation of H_2O to H_2O_2. For both ORR and WOR to proceed efficiently, the photogenerated charge carriers must possess appropriate redox potentials that meet the thermodynamic criteria of the respective reactions.

The reduction of O_2 in photocatalytic systems typically proceeds *via* the following pathways [47–50]:

(a) Oxygen reduction reaction (ORR) pathways

Two-electron reduction (2e⁻ ORR):

$$O_2 + 2H^+ + 2e^- \rightarrow H_2O_2 \left(E^0 = +0.68\,V\,vs.\,NHE\right) \quad (1)$$

One-electron reduction (1e⁻ ORR):

$$O_2 + e^- \rightarrow \cdot O_2^- \left(E^0 = -0.33\,V\,vs.\,NHE\right) \quad (2)$$

$$\cdot O_2^- + e^- + 2H^+ \rightarrow H_2O_2 \left(E^0 = +1.44\,V\,vs.\,NHE\right) \quad (3)$$

The competing reaction in this process is:

$$O_2 + 4e^- + 4H^+ \rightarrow 2H_2O \left(E^0 = +1.23\,V\,vs.\,NHE\right) \quad (4)$$

(b) Water oxidation reaction (WOR) pathways [51,52]

Two-electron water oxidation (2e⁻ WOR):

$$2\,H_2O + 2h^+ \rightarrow 2\,H_2O_2 + 2H^+ \left(E^0 = +1.76\,V\,vs.\,NHE\right) \quad (5)$$

One-electron water oxidation (1e⁻ WOR):

$$H_2O + h^+ \rightarrow \cdot OH \left(E^0 = +2.73\,V\,vs.\,NHE\right) \quad (6)$$

$$2 \cdot OH \rightarrow H_2O_2 \left(E^0 = +1.14\,V\,vs.\,NHE\right) \quad (7)$$

The main competing reaction in this process is:

$$2H_2O + 4h^+ \rightarrow O_2 \left(E^0 = +1.23\,V\,vs.\,NHE\right) \quad (8)$$

The ORR involved in H_2O_2 synthesis proceeds *via* a two-electron transfer mechanism, which can be conceptualized either as a direct two-electron process (Eq. 1) or as a sequential two-step single-electron process (Eqs. 2 and 3). In the latter pathway, the superoxide radical anion ($\cdot O_2^-$) serves as a key intermediate species. Notably, the redox potential of the O_2/H_2O_2 couple (0.68 V *versus* the normal hydrogen electrode, NHE) is more positive than that of the $O_2/\cdot O_2^-$ couple (-0.33 V *vs.* NHE), suggesting, from a thermodynamic standpoint, a greater likelihood for the direct two-electron pathway to predominate. During photocatalytic O_2 reduction, a competing reaction exists wherein O_2 undergoes further reduction to water (H_2O) *via* photogenerated electrons (Eq. 4). Given that the redox potential of the O_2/H_2O couple (1.23 V *vs.* NHE) exceeds that of the O_2/H_2O couple, the four-electron ORR pathway is thermodynamically more favorable.

Similarly, the WOR on photocatalysts can proceed through multiple electron transfer routes, including four-electron, two-electron, and one-electron pathways (Eqs. 5-7). The two-electron WOR pathway can be further subdivided into an indirect two-step single-electron transfer mechanism (Eqs. 6 and 7) and a direct one-step two-electron process (Eq. 5). Thermodynamically, the direct two-electron pathway is preferred; however, kinetically, the indirect mechanism tends to dominate. For effective H_2O_2 generation *via* the two-electron WOR route, the valence band edge of the photocatalyst must be positioned more positively than + 1.76 V *versus* NHE to satisfy thermodynamic criteria. In contrast, the four-electron WOR pathway is thermodynamically more advantageous, thereby favoring oxygen evolution over H_2O_2 production.

Photocatalysts typically demonstrate low adsorption energies for oxygen, which facilitates the desorption of reaction products [53]. Overall, the two-step single-electron transfer mechanism is kinetically more favorable. Concurrently, O_2 readily interacts with photogenerated holes to form singlet oxygen species ($^1O_2$, $\cdot O_2^-/^1O_2$ 0.34 V *vs.* NHE), resulting in a reduction of H_2O_2 yield. Analogous to the two-electron ORR, the actual efficiency of the two-electron WOR is governed by the interplay between thermodynamic driving forces and kinetic energy barriers. This reaction can proceed *via* two potential pathways: a direct two-electron transfer or a stepwise single-electron transfer, with the stability of intermediate species critically determining the preferred reaction route.

The formation and stability of key intermediates such as superoxide radicals ($\cdot O_2^-$), hydroperoxyl species (*OOH), and singlet oxygen ($^1O_2$), alongside oxygen adsorption and activation behaviors, charge separation efficiency, and interfacial reaction kinetics, collectively exert a decisive influence on the rate and selectivity of H_2O_2 production. It is imperative to modulate the electron density at the catalyst's active sites to ensure that the bond energies align with the energy barriers required for efficient two-electron transfer, thereby minimizing side reactions associated with excessively strong or weak bonding. Furthermore, in photocatalytic systems, promoting the directional transfer of photogenerated charge carriers-electrons to O_2 in ORR or holes to H_2O in WOR-while suppressing charge recombination is essential to maintain sufficient charge availability for two-electron processes. An ideal photocatalyst should exhibit an appropriate band structure, a high density of surface-active sites, favorable oxygen affinity, and controllable electron transfer pathways to optimize performance.

2. The applications and modification strategies of g-C_3N_4 in the photocatalytic H_2O_2 production

In the domain of photocatalytic research, the efficient photocatalyst is one of the important cores. But the developments of semiconductor photocatalysts exhibit high efficiency, robust stability, and the capability to utilize a broad spectrum of solar radiation remains a significant and ongoing challenge. A variety of photocatalysts have been extensively studied, demonstrating promising performance in specific reactions; these include metal oxides [54–62], sulfides [63–68], oxynitrides [69], metal-organic frameworks (MOF) [70–74], covalent organic frameworks (COF) [75–77], and polymer [78,79], *etc.* Nevertheless, they still share several fundamental limitations, such as restricted visible-light absorption, rapid recombination of photogenerated charge carriers, low quantum yield, and inadequate long-term chemical stability [60,61,80]. These issues significantly hinder their practical applications on a larger scale.

A prototypical example is titanium dioxide (TiO_2), one of the most extensively investigated photocatalysts. With a bandgap of approximately 3.2 eV, TiO_2 predominantly absorbs ultraviolet light, which accounts for less than 5% of the solar spectrum, and exhibits minimal photocatalytic activity under visible light [81–87]. Although strategies such as elemental doping, composite formation, and surface sensitization have been employed to enhance its light-harvesting capabilities, these modifications cannot fully surmount the fundamental absorption limitations imposed by its wide bandgap. Photostability constitutes another critical issue. Narrow-bandgap materials such as cadmium sulfide (CdS) and tantalum oxynitride (TaON), which possess favorable band alignments for visible-light absorption, are prone to photo-corrosion and chemical degradation [88]. For example, under illumination, photogenerated holes in CdS can oxidize sulfide ions to sulfate, causing irreversible structural damage [89]. Similarly, certain nitride-based photocatalysts experience surface oxidation or lattice instability upon prolonged light exposure, leading to rapid declines in catalytic activity over successive cycles. Additionally, phenomena such as light-induced leaching of active species and surface reconstruction further undermine the structural integrity and long-term durability of these materials.

Multielectron processes, such as overall water splitting, impose more rigorous demands on photocatalysts [90–93]. The photocatalytic material must not only provide active sites for both proton reduction and water oxidation but also effectively reduce the substantial overpotentials associated with hydrogen and oxygen evolution reactions [94–96]. These requirements establish stringent criteria concerning the band structure, charge transport characteristics, and surface reaction kinetics of photocatalysts. At present, only a limited number of systems concurrently fulfill the criteria of broad spectral absorption, efficient charge separation, and exceptional stability [97,98]. Consequently, progress in this domain necessitates the design and synthesis of novel photocatalytic materials that can harness a wider spectrum of solar radiation, promote effective charge separation and transfer, and sustain durable performance under chemically demanding conditions. Pursuing this approach is critical for realizing efficient, stable, and scalable solar energy conversion technologies.

Recently, g-C_3N_4 has garnered considerable interest as a potential photocatalyst for H_2O_2 synthesis and become a hot research topic in recent years (Fig. 2), due to its unique two-dimensional layered structure, metal-free composition, ability to absorb visible light, and adjustable electronic properties [99–102]. The performance comparison of some modified g-C_3N_4-based photocatalysts for H_2O_2 production and relevant references are shown in Table 1. The conduction band potential of g-C_3N_4 is approximately -1.3 V *vs.* NHE [103], which thermodynamically facilitates the oxygen reduction reaction (Fig. 1b). Additionally, the intrinsic g-C_3N_4 material absorbs mainly in the UV–visible region, yet its visible-light response remains insufficient, restricting its photocatalytic efficiency [104,105]. Therefore, improving photocatalysts capable of effectively utilizing visible light is crucial for enhancing solar-energy conversion. Although nearly 48% of solar irradiation lies below 700 nm, the limit constrains the theoretical conversion efficiency, meaning that extending the absorption range alone does not guarantee higher photocatalytic performance. Furthermore, the practical utilization of g-C_3N_4 is impeded by several inherent drawbacks, including a high exciton binding energy that hampers effective charge carrier separation, limited oxygen adsorption capacity, a low density of states within the conduction band region, a scarcity of catalytically active sites, and the propensity of H_2O_2 to decompose under reaction conditions.

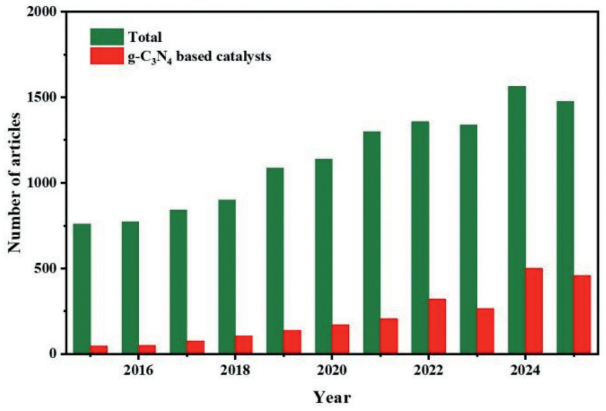


Fig. 2. The number of articles on photocatalytic H_2O_2 generation searched from web of science from 2015 to 2025.

From view of the structure, the layered structure held together by weak van der Waals forces provides poor in-plane conductivity and promotes rapid electron–hole recombination, further exacerbated by abundant intrinsic defect states associated with lone-pair nitrogen atoms that act as charge-trapping centers. The low specific surface area of bulk g-C_3N_4 ($< 10\ m^2/g$) leads to a scarcity of catalytically active sites and weak adsorption of O_2 and the OOH* intermediate, which slows the kinetics of the $2e^-$ oxygen reduction pathway required for selective H_2O_2 formation. In addition, its conduction band is sufficiently negative to trigger competing $4e^-$ ORR or promote further reduction and decomposition of the generated H_2O_2, while the valence band position (~1.4 V *vs.* RHE) is not positive enough to thermodynamically drive the $2e^-$ water oxidation pathway, preventing a synergistic oxidation contribution to H_2O_2 accumulation [106–109]. The combination of restricted visible-light absorption, short carrier lifetimes, limited active-site density, weak O_2 activation capability, and competing redox pathways collectively results in the inherently low H_2O_2 yield of g-C_3N_4, making rational structural modification essential for achieving high photocatalytic efficiency.

While the fundamental mechanisms provide a theoretical foundation, translating these principles into efficient photocatalytic systems requires deliberate material design. To enhance the photocatalytic performance of g-C_3N_4, researchers have developed multi-dimensional optimization strategies focusing on its electronic structure and interface chemistry (Fig. 1c). Approaches such as defect engineering, heteroatom doping, single-atom loading, π-π interaction modification, junction construction, colloidal dispersion, and multi-interface synergy have been proposed [110–113]. These strategies not only improve the light absorption capacity and charge carrier separation efficiency of g-C_3N_4, but also regulate the O_2 adsorption mode, the formation and stability of *OOH intermediates, proton transfer pathways, and H_2O_2 desorption behav-

Table 1
Performance comparison of some modified g-C_3N_4-based photocatalysts for H_2O_2 production.

Authors (year)	Catalyst	Modification strategy	Light source	H_2O_2 production activity	Enhancement factor (*vs.* pristine CN)	AQY/wavelength	Electron donor	Ref.
Yang *et al.* (2023)	$A_{0.05}$CN	Carbon doping & surface -OH	Visible ($\lambda \geq 420$ nm)	3.6 mmol g^{-1} h^{-1}	3.5 ×	Not available	Pure water	[130]
Zhang *et al.* (2024)	s-B_xCN	Carbon doping, N vacancies, -C≡N	Visible light	54.2 μmol L^{-1} h^{-1}	Not available	Not available	Pure water	[131]
Xu *et al.* (2025)	KLCN	Lignin-derived carbon ring embedding & N defects	Visible light	266.82 μmol/L	6.93 ×	Not available	Isopropanol	[132]
Wei *et al.* (2018)	OCN-500	Oxygen doping (C-O-C/–OH)	Visible light	730 μmol / 5h	3.5 ×	28.5 %@365 nm, 10.2 %@420 nm	Isopropanol	[133]
Yu *et al.* (2023)	PCN-D	Dual-site P doping (bay & corner)	Visible light	413.85 μmol L^{-1} h^{-1}	>6 ×	Not available	Isopropanol	[134]
Ma *et al.* (2024)	BCN-450	B doping (Frustrated Lewis Pairs)	Visible light	51008 μmol L^{-1} g^{-1} h^{-1}	12.4 ×	Not available	Ethanol	[135]
Zhang *et al.* (2023)	CN-1.0	S doping & N vacancies	Xenon lamp	293.2 μmol/L / 4 h	2.4 ×	Not available	Ethanol	[136]
Liu *et al.* (2021)	B-CNT	B/P/S co-doping, nanotube	Simulated sunlight	1830.98 μmol/L / 4 h	2 ×	Not available	Isopropanol	[137]
Habarugira *et al.* (2024)	10SD-CN	Na doping & N defects	Visible light	297.2 μmol L^{-1} h^{-1}	9.8 ×	1.29 %@420 nm	Isopropanol	[138]
Wu *et al.* (2020)	ACNN	K^+/Na^+ doping & N vacancies	Visible ($\lambda \geq 420$ nm)	10.2 mmol g^{-1} h^{-1}	89.5 ×	30.7 %@429 nm	Isopropanol	[139]
Chen *et al.* (2021)	5Cv@g-C_3N_4	Cyano defects & Na doping, porous	Visible ($\lambda \geq 420$ nm)	7.01 mmol L^{-1} h^{-1}	220 ×	9.58 %@420 nm	Ethanol	[140]
Zhang *et al.* (2020)	AKMT	S/K co-doping	Visible light	4.1 mmol/L / 3 h	Not available	100 %@450 nm	Ethanol	[145]
Wang *et al.* (2024)	$Na_{1.2}$-$P_{0.2}$-CN	P/Na co-doping	Visible light	3001.64 μmol g^{-1} L^{-1} / 100 min	62 ×	Not available	Isopropanol	[146]
Wu *et al.* (2022)	GCN	Carbon defects, flower-like	Xenon lamp ($\lambda >$ 420 nm)	21.59 mmol L^{-1} g^{-1} h^{-1}	5 ×	Not available	Isopropanol	[149]
Zhang *et al.* (2022)	Nv-C≡N-CN	N vacancies & -C≡N groups	Visible ($\lambda \geq 420$ nm)	3093 μmol g^{-1} h^{-1}	8.7 ×	36.2 %@400 nm	Isopropanol	[152]
Li *et al.* (2023)	SCN2	S doping, -NH_2/-CH_3 edge groups	Visible ($\lambda \geq 420$ nm)	416.7 μmol g^{-1} h^{-1}	10 ×	31.6 %@365 nm	Pure water	[150]
Zeng *et al.* (2025)	BPMC-Vs	B/P co-doping & N defects	Visible ($\lambda \geq 420$ nm)	650.7 μmol g^{-1} h^{-1}	9.9 ×	39.1 %@420	Isopropanol	[151]
Chen *et al.* (2023)	CNT	Crystallinity enhancement (Molten salt)	AM 1.5	2.48 mmol g^{-1} h^{-1}	5.8 ×	22 %@ 00 nm	Isopropanol	[153]
Zhong *et al.* (2024)	CN-K(1:6)	K doping, High crystallinity	LED	7.8 mmol L^{-1} h^{-1}	220 ×	5.17 %@420 nm	Isopropanol	[154]
Li *et al.* (2024)	BTOCN2	$Bi_4Ti_3O_{12}$/g-C_3N_4 S-scheme	Simulated sunlight	1650 μmol g^{-1} h^{-1}	2.8 ×	0.36 %@420 nm	Methanol	[173]
Zhang *et al.* (2023)	3$CuInS_2$/PCN	$CuInS_2$/PCN S-scheme	Visible light	1247.6 μmol g^{-1} h^{-1}	11.6 ×	16.0 %@420 nm	Isopropanol	[174]
Chen *et al.* (2023)	homo-CN	Homojunction (OH-rich/OH-defective)	Xenon lamp ($\lambda \geq$ 420 nm)	508.4 μmol L^{-1} L^{-1}	4.5 ×	2.1 %@500 nm	Ethanol	[179]
Zhang *et al.* (2024)	CN-NH_4-NaK	Homojunction (Order-Disorder)	Visible ($\lambda \geq 420$ nm)	16675 μmol g^{-1} h^{-1}	158 ×	34.3 %@395 nm, 28.4 %@420 nm	Isopropanol	[181]
Foo *et al.* (2025)	CCN-550	Homojunction (PHI/PTI), K^+/Li^+, -C≡N	Visible ($\lambda \geq 420$ nm)	5838.91 μmol L^{-1} h^{-1}	31.7 ×	11.57 %@420 nm	Benzyl alcohol	[184]
Hou *et al.* (2024)	CoO_x-NvCN	N vacancies & CoO_x clusters	Visible ($\lambda \geq 420$ nm)	244.8 μmol L^{-1} h^{-1}	12.1 ×	5.73 %@420 nm	Pure water	[190]
Jing *et al.* (2024)	CoO_x-BCN-FeOOH	B doping, FeOOH & CoO_x clusters	Visible ($\lambda \geq 420$ nm)	0.34 mmol g^{-1} h^{-1}	30 ×	8.36 %@420 nm	Pure water	[191]
Zhang *et al.* (2023)	Ni-SAPs/PuCN	Ni single-atom (Ni-N_3)	Visible ($\lambda \geq 420$ nm)	342.2 μmol L^{-1} h^{-1}	20.7 ×	10.9 %@420 nm	Pure water	[143]
Su *et al.* (2021)	Sb-SAPC15	Sb single-atom (Sb-N)	Visible ($\lambda >$ 420 nm)	6.2 mg L^{-1} h^{-1}	248 ×	17.6 %@420 nm	Pure water	[144]

ior from the intrinsic structural level, thereby significantly boosting catalytic activity and product selectivity [114–117]. Particularly in recent years, the H_2O_2 production rate of high-performance g-C_3N_4 catalysts has increased from several hundred μmol g^{-1} h^{-1} in the early stage to 10–50 mmol g^{-1} h^{-1}, with quantum efficiency exceeding 30 %, indicating that photocatalytic H_2O_2 synthesis is becoming increasingly mature for practical application. Nonetheless, current systems continue to face significant challenges, including limited universality in structural regulation, difficulties in *in situ* observation of reaction intermediates, inadequate long-term stability, and obstacles to large-scale fabrication, all of which impede the commercial advancement of photocatalytic H_2O_2 technologies.

In response, this paper centers on g-C_3N_4 and provides a systematic review and in-depth analysis of the evolution of reaction mechanisms, material design strategies, and performance optimization pathways for photocatalytic H_2O_2 production in recent years. The scope of this work encompasses: (1) Fundamental reaction pathways and surface dynamic processes involved in photocatalytic H_2O_2 generation; (2) the effects of intrinsic and modified structural regulation of g-C_3N_4 on catalytic performance; (3) key challenges and limitations in current research; and (4) prospects for future material design, device integration, and application development. This study aims to offer a theoretical foundation and research reference to facilitate the development of a new generation of efficient, environmentally friendly, and cost-effective photocatalytic H_2O_2 technologies.

2.1. Doping

Doping represents a straightforward yet effective approach for optimizing the performance of g-C_3N_4 in photocatalytic application. Introducing metal or non-metal dopants can significantly modulate the electronic structure of the material, thereby improving its catalytic activity [118–125]. Such modifications induce profound changes in the electronic configuration through interactions between dopant atoms and the carbon/nitrogen framework [126–129]. Specifically, doping narrows the band gap by introducing in-gap states or facilitating orbital hybridization, while also tuning the energies of the valence band maximum (VBM) and conduction band minimum (CBM) to optimize redox potentials. Furthermore, the density of states near the Fermi level is altered, enhancing charge carrier density and conductivity. Notably, the reconstruction of the surface electronic structure promotes the adsorption of reactants and reduces the activation energy barriers for key reaction intermediates. Based on the nature of the incorporated elements, doping strategies for g-C_3N_4 can be categorized into non-metal doping, metal doping, and co-doping. Each approach contributes synergistically to enhance light absorption, facilitate charge separation, and improve interfacial catalytic efficiency. These mechanisms have been corroborated through comprehensive experimental analyses, including spectroscopic characterization, transient photoelectrochemical techniques, and detailed reaction pathway studies.

2.1.1. Non-metal doping

2.1.1.1. Carbon doping. Carbon doping is commonly achieved by increasing the C/N ratio within the g-C_3N_4 framework or introducing carbon-rich organic precursors to partially substitute nitrogen sites. This approach enhances the π-electron density and increases the density of states in the conduction band, thereby facilitating photogenerated electron transfer toward the oxygen reduction pathway. Additionally, the incorporation of carbon can lead to the formation of C-terminal defects and non-conjugated groups, which further modulate the conduction band edge-promoting O_2 adsorption and stabilizing reactive intermediates. These modifications collectively contribute to an extended charge carrier lifetime.

For example, Yang *et al*. engineered dual defects-namely carbon doping and surface hydroxyl (-OH) modification-by adjusting the acetylacetone to urea precursor ratio [130]. The optimized sample $A_{0.05}$CN demonstrated a H_2O_2 production rate of 3.6 mmol g^{-1} h^{-1} under visible light irradiation ($\lambda \geq 420$ nm), which is 3.5 times greater than that of pristine g-C_3N_4 (Figs. 3a-d). Additionally, the selectivity increased from 60 % to 85 %. Integrated experimental and theoretical investigations indicated that carbon doping enhanced oxygen adsorption and activation at N_2C sites, whereas surface hydroxyl groups promoted charge carrier diffusion and inhibited recombination. The observed narrowing of the band gap to 2.56 eV, the enlarged surface area, and a significant electron transfer number ($n \approx 2.0$) collectively corroborate the improved two-step single-electron oxygen reduction mechanism.

In another approach, Zhang *et al*. synthesized carbon-doped, defect-rich g-C_3N_4 (s-B≡CN) *via* supramolecular pre-assembly and thermal polymerization [131]. Incorporating barbituric acid yielded a nest-like porous structure enriched with N vacancies and –C≡N groups, which broadened visible light absorption and improved charge separation. The material achieved an H_2O_2 production rate of 108.4 μmol/L within 2 h in pure water, attributed to the synergistic effect of strengthened $2e^-$ ORR (*via* $\cdot O_2^-$) and hole-driven water oxidation. Furthermore, the *in-situ* generated H_2O_2 enabled efficient degradation of 4-chlorophenol *via* a photo-self-Fenton process, highlighting potential practical applications. Xu *et al*. employed a co-modification strategy using lignin and KOH to embed carbon rings and induce nitrogen defects (cyano groups and N vacancies) in KLCN (Figs. 3e-g) [132]. This synergistic incorporation resulted in an H_2O_2 yield 6.93 times greater than that of the unmodified catalyst, with mechanistic studies confirming the critical role of $\cdot O_2^-$ intermediates in the two-step single-electron reduction pathway.

Current studies have demonstrated that carbon doping enhances the photocatalytic activity of g-C_3N_4 through band structure engineering, improved charge carrier kinetics, and enhanced surface adsorption of reactants. A key advantage is the concurrent activation of both oxygen reduction and water oxidation pathways, providing a versatile strategy for designing efficient photocatalytic systems for H_2O_2 production.

2.1.1.2. Oxygen doping. Wei *et al*. developed an oxygen-enriched carbon nitride polymer (OCN) with enhanced photocatalytic performance for H_2O_2 generation (Figs. 3h-k) [133]. DFT simulations indicated that incorporating C-O-C groups considerably lowered the energy barrier for forming 1,4-endoperoxide intermediates by 10.5 kcal/mol compared to -NH_2 groups, thus favoring selective oxygen reduction. The material, labeled OCN-500, was synthesized through calcination at 500 °C in air using dicyandiamide and ammonium paratungstate as precursors. This process introduced C-O-C and -OH functional groups, increased the specific surface area, and narrowed the band gap. Under O_2-saturated conditions in pure water, OCN-500 exhibited an H_2O_2 production rate of 730 μmol over 5 h, representing a 3.5-fold enhancement over unmodified g-C_3N_4. The catalyst also demonstrated high apparent quantum yields (28.5 % at 365 nm and 10.2 % at 420 nm) and exceptional stability over 20 h. RDE and EPR analyses corroborated the dominance of the two-electron oxygen reduction pathway ($n = 2.54$) and the presence of radical intermediates (ROO·/RO·), respectively, with the proposed 1,4-endoperoxide mechanism further supported by DFT.

2.1.1.3. Phosphorus doping. A dual-site phosphorus doping strategy was introduced by Yu *et al*. to markedly improve the photocatalytic H_2O_2 production activity of g-C_3N_4 (Figs. 3l-o) [134]. Through thermal polymerization, P atoms were selectively incorporated at both bay and corner sites of the heptazine framework, effectively breaking electron localization symmetry and reducing

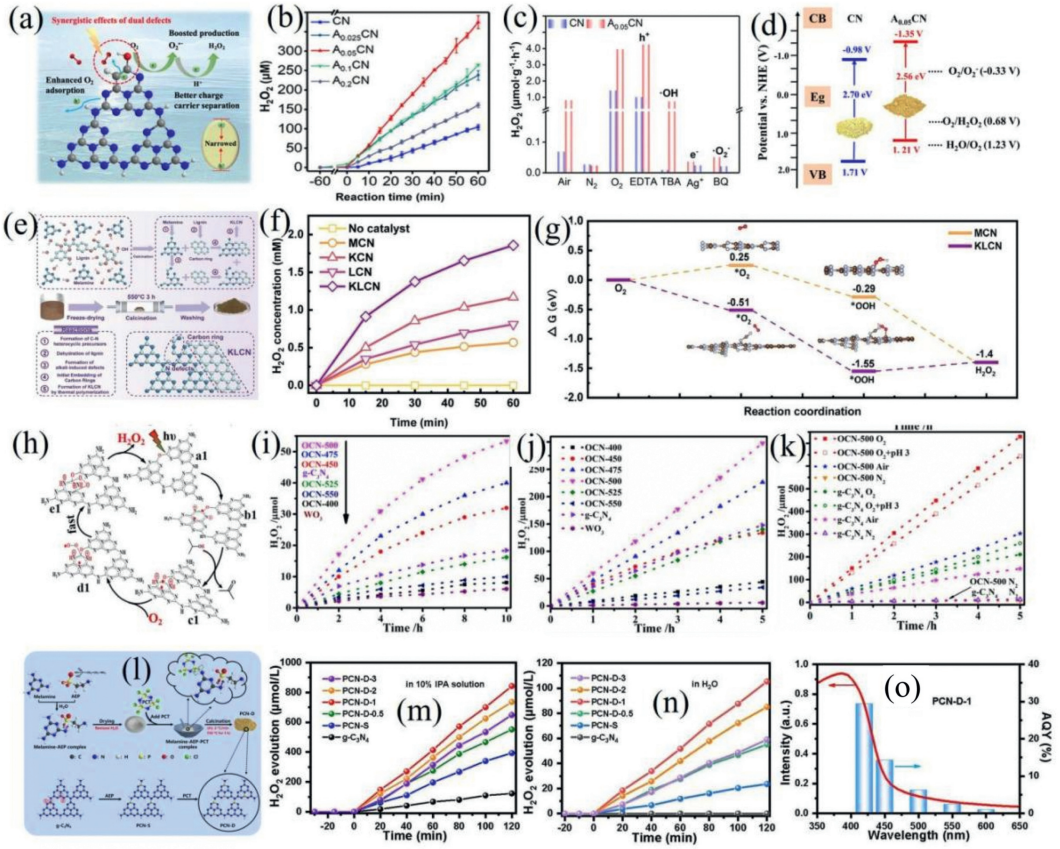


Fig. 3. (a) Schematic diagram of reaction mechanism. (b) The H_2O_2 production under visible light irradiation. (c) Effects of reactive species scavengers. (d) Schematic illustration of ORR and WOR in CN and $A_{0.05}CN$. Reproduced with permission [130]. Copyright 2023, American Chemical Society. (e) The preparation technical route. (f) Photocatalytic production of H_2O_2 under simulated sunlight. (g) Free energy diagrams of ORR steps for MCN and KLCN. Reproduced with permission [132]. Copyright 2025, Elsevier B.V. (h) The mechanism of OCN model (C-O-C) photocatalytic O_2 reduction. (i) The photocatalytic generation of H_2O_2 in O_2 saturated pure water under visible light. (j) The photocatalytic generation of H_2O_2 with 10% isopropyl alcohol under visible light irradiation with air atmosphere. (k) The photocatalytic generation of H_2O_2 with 10% isopropyl alcohol under different atmosphere and pH under visible light irradiation. Reproduced with permission [133]. Copyright 2018, Royal Society of Chemistry. (l) Schematic diagram of the PCN-D sample synthesis. (m) Time course of photocatalytic H_2O_2 generation of PCN-D samples in 10% IPA solution, and (n) in pure water. (o) Wavelength-dependent AQY of PCN-D-1 sample. Reproduced with permission [134]. Copyright 2023, Elsevier B.V.

exciton binding energy. This resulted in an exciton dissociation efficiency surge from 0.59% to 11.9%, alongside a 13-fold increase in charge carrier concentration and a 7-fold mobility improvement. The optimized catalyst (PCN-D) achieved an H_2O_2 generation rate of 413.85 μmol L^{-1} h^{-1} under visible light which is 6 times that of pristine g-C_3N_4 and performed robustly in both pure water and seawater. Mechanistic studies revealed that corner-site P doping enhances O_2 adsorption and activation, while bay-site doping facilitates charge delocalization and separation, collectively promoting an efficient 2e^- ORR.

2.1.1.4. Boron doping. Ma *et al.* employed boron doping to construct frustrated Lewis pairs (FLPs) within the carbon nitride matrix, significantly boosting H_2O_2 production (Figs. 4a-d) [135]. The FLPs consist of boron Lewis acid sites and nitrogen Lewis base sites adjacent to cyano groups. The introduced B atoms created spin-polarized empty orbitals, improving visible light absorption and charge separation. The FLP structure preferentially activated ethanol *via* a "push–pull" mechanism rather than direct oxygen reduction. DFT studies indicated a reduction of the ethanol dissociation barrier to 0 eV, leading to H_2O_2 formation through synergistic action of $\cdot O_2^-$ and $^1O_2$ intermediates. In a 10% ethanol solution, the catalyst (BCN-450) attained a remarkable H_2O_2 production rate of 51008 μmol L^{-1} g^{-1} h^{-1}, 12.4 times that of the baseline, with consistent performance over five cycles. *In-situ* IR spectroscopy confirmed ethanol activation to aldehyde species, underscoring the role of FLPs in altering reaction selectivity and pathway efficiency.

2.1.1.5. Sulfur doping. Zhang *et al.* concurrently introduced sulfur dopants and nitrogen vacancies into g-C_3N_4 *via* hydrothermal etching with ammonium persulfate, coupled with morphological control to obtain a porous fluffy architecture (Figs. 4e-g) [136]. This dual-defect system synergistically optimized the electronic structure, and the 27-fold enlargement of specific surface area significantly improved O_2 adsorption capacity. The modified catalyst yielded 293.2 μmol/L H_2O_2 within 4 h, 2.4 times higher than pristine g-C_3N_4, with high selectivity for the two-electron pathway. Sulfur doping induced a valence band positive shift, while nitrogen vacancies enhanced charge separation. The porous framework further facilitated mass transfer and exposure of active sites. Nevertheless, the system's reliance on ethanol as a sacrificial agent-causing a 53% activity drop in its absence-highlights a limitation for practical application and underscores the need for developing sacrificial-agent-free configurations.

2.1.1.6. Multielement doping. Liu *et al.* prepared boron/phosphorus/sulfur-doped g-C_3N_4 nanotubes (B/P/S-CNT) *via* a template-free hydrothermal-thermal polymerization synergistic strategy, enabling efficient photocatalytic H_2O_2 synthesis (Figs. 4h-j) [137]. A melamine-cyanuric acid supramolecular self-assembly was used to form a tubular precursor, which was then thermally

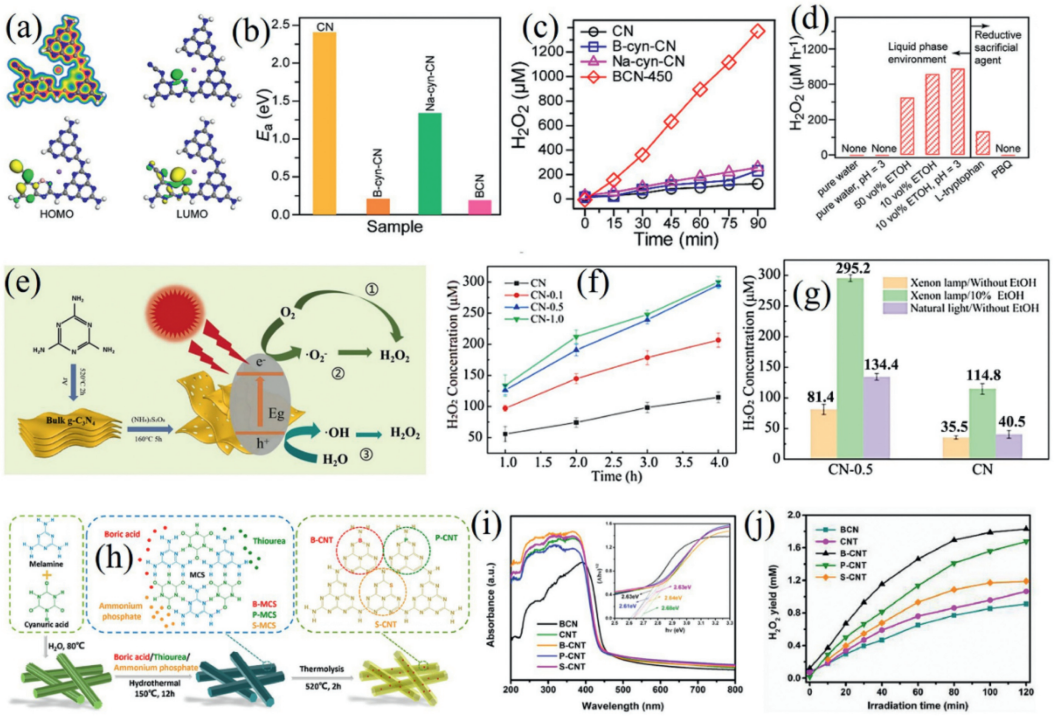


Fig. 4. (a) Electron density, spin density, HOMO, and LUMO of BCN. (b) Energy barriers (E_a) of the rate-determining steps on various samples. (c) Time-dependent photocatalytic H_2O_2 production of different CN-based samples. (d) H_2O_2 production rate of BCN-450 with different reductive scavengers. Reproduced with permission [135]. Copyright 2024, American Chemical Society. (e) The possible mechanism for H_2O_2 production over CN-0.5 catalyst, (f) H_2O_2 generation rates of CN, CN-0.1, CN-0.5, and CN-1.0 catalysts. (g) Concentration of the produced H_2O_2 under different conditions. Reproduced with permission [136]. Copyright 2023, Elsevier B.V. (h) Schematic illustration for catalyst fabrication. (i) The optical properties of samples. (j) Photocatalytic H_2O_2 generation performance of different samples. Reproduced with permission [137]. Copyright 2021, Elsevier B.V.

polymerized at 520 °C to obtain a porous nanotube structure (BET specific surface area was 6.7 times that of bulk g-C_3N_4). Its hierarchical pores significantly promoted mass transfer and light harvesting. Simultaneously, the co-doping of non-metallic elements B, P, and S optimized the electronic structure, shifting the conduction band negatively by 0.15 eV and improving charge carrier separation efficiency. The optimal B-CNT sample achieved a maximum H_2O_2 yield of 1830.98 μmol/L, 4 h, twice that of bulk g-C_3N_4. Experimental results confirmed that the activity difference originated from the regulatory strength of doped elements on the reduction potential and the enhanced light reflection and absorption by the tubular structure. The two-electron oxygen reduction pathway dominated the H_2O_2 generation process, and isopropanol as a sacrificial agent provided key protons.

2.1.2. Metal doping

Metal doping introduces foreign metal atoms into the g-C_3N_4 matrix, effectively modulating its electronic structure and surface properties to enhance photocatalytic H_2O_2 production. Habarugira *et al.* developed a one-step copolymerization approach using sodium dicyanamide to fabricate sodium-doped carbon nitride with nitrogen vacancies (SD-CN) [138]. The introduced sodium disrupted the triazine unit ordering, leading to a wrinkled morphology. Characterization confirmed the coexistence of cyano groups, nitrogen vacancies, and Na incorporation, with the band gap narrowing to 2.75 eV (Figs. 5a-d). The optimized catalyst exhibited an H_2O_2production rate of 297.2 μmol L^{-1} h^{-1}, which is 9.8 times higher than pristine g-C_3N_4 and obtained an AQE of 1.29 % at 420 nm, and 90 % stability retention over 8 cycles. Mechanism studies indicated cyano groups aided charge separation, while nitrogen vacancies promoted O_2 adsorption, collectively favoring the two-electron ORR pathway as evidenced by ESR and RDE (n = 1.77). Despite these merits, the low specific surface area (3.40 m^2/g) and limited anti-interference ability in real water environments necessitate further improvements in mass transfer and practicality.

Wu *et al.* employed a eutectic salt ionothermal etching strategy (NaCl/KCl) to co-incorporate alkali metals (K^+/Na^+) and nitrogen vacancies into g-C_3N_4 (Figs. 5e-g) [139]. The dual modification narrowed the band gap from 2.85 eV to 2.63 eV and enhanced charge separation efficiency by 6.2 times. The best-performing ACCN sample achieved a remarkable H_2O_2 yield of 10.2 mmol g^{-1} h^{-1}, 89.5 times that of the pristine material, with an apparent rate constant increased by 149 times and an AQE of 30.7 % at 429 nm. Nitrogen vacancies functioned as electron traps to facilitate charge separation, while alkali metal doping optimized the band structure *via* charge compensation from -O^- and -C≡N groups. Nevertheless, the system's dependency on isopropanol as a sacrificial agent and modest cycling stability represent challenges for sustainable application.

Chen *et al.* designed a cyano-rich, honeycomb-structured carbon nitride (C_v@g-C_3N_4) *via* a NaCl-assisted calcination route (Figs. 5h-o) [140]. The material concurrently introduced cyano defects and sodium doping, which reduced the band gap through newly formed defect levels and enhanced O_2 adsorption *via* improved charge polarization. A NaN_3-like coordination environment further promoted carrier separation and stabilized superoxide intermediates. Combined with a porous morphology for improved surface area, the catalyst delivered an H_2O_2 production rate of 7.01 mmol L^{-1} h^{-1} under visible light-220 times higher than conventional g-C_3N_4-with an AQE of 9.58 % at 420 nm. It also demonstrated broad pH adaptability (3–12) and good cycling stability, maintaining 5 mmol L^{-1} h^{-1} after 5 cycles.

Photocatalytic activity is considered the cumulative result of surface reactions between active sites on the catalyst and reactants. However, identifying the dynamic structural evolution of active sites during photocatalytic surface reactions and clarifying the cor-

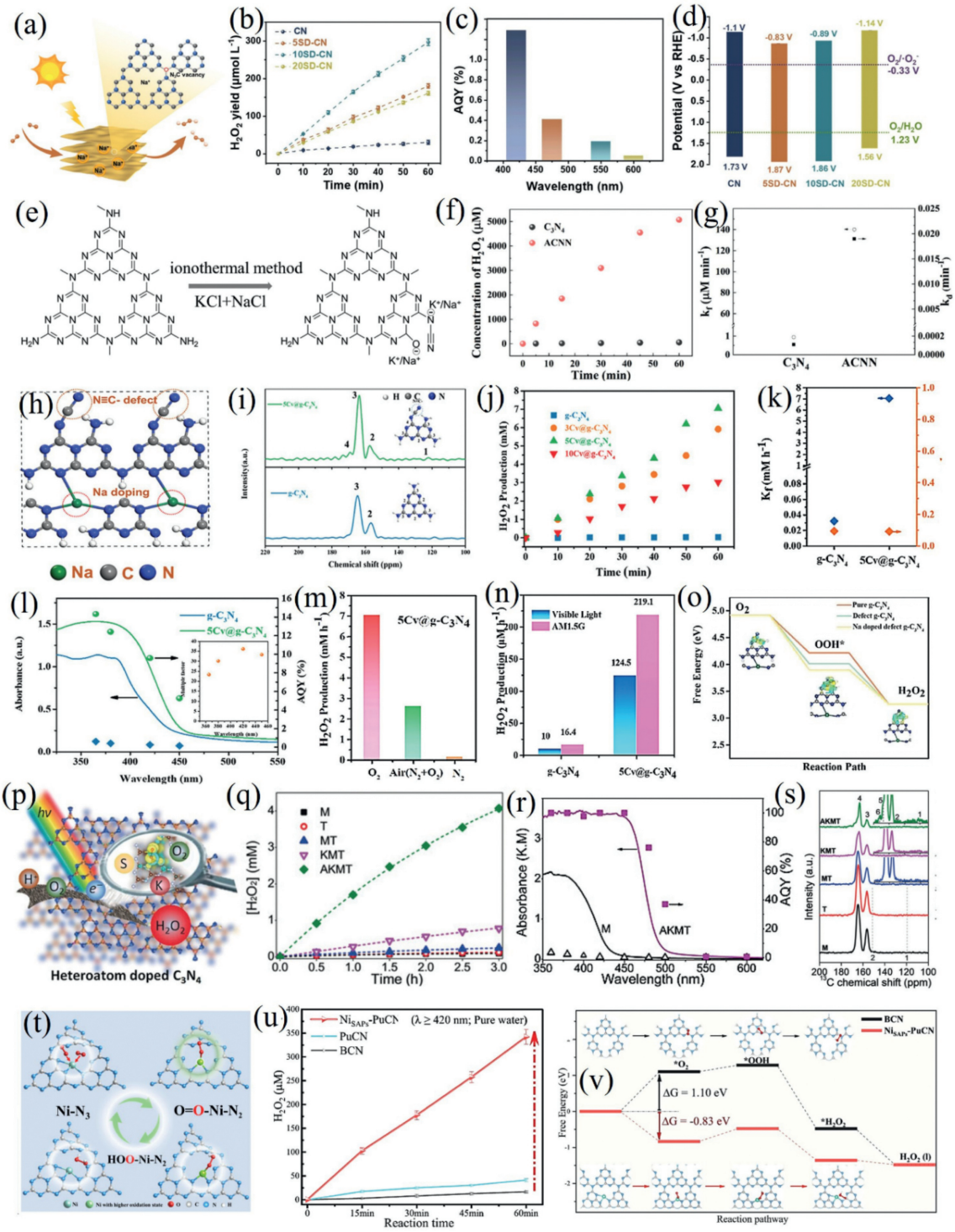


Fig. 5. (a) Schematic illustration of SD-CN catalyst structure and H_2O_2 generation. (b) H_2O_2 production rates of different SD-CN and CN samples. (c) Apparent quantum yield (AQY) of 10SD-CN, and (d) the electronic band structure. Reproduced with permission [138]. Copyright 2024, Elsevier B.V. (e) Schematic illustration of the preparation procedure. (f) H_2O_2 production of ACNN and C_3N_4 under visible light irradiation. (g) Formation (k_f) and decomposition (k_d) kinetics constant of H_2O_2 over ACNN and C_3N_4. Reproduced with permission [139]. Copyright 2020, American Chemical Society. (h) Schematic of proposed structure of Cv@g-C_3N_4. (i) The solid-state nuclear magnetic resonances (NMR) spectra ^{13}C of g-C_3N_4 and 5Cv@g-C_3N_4. (j) Catalytic performance of Cv@g-C_3N_4. (k) Rate constant over g-C_3N_4 and 5Cv@g-C_3N_4. (l) The apparent quantum yield (AQY). (m) The H_2O_2 production rate with different conditions. (n) H_2O_2 generation rate in the O_2-saturated pure water. (o) The free energy results. Reproduced with permission [140]. Copyright 2021, Wiley. (p) Proposed reaction mechanism of AKMT catalyst. (q) H_2O_2 production performance at pH 3. (r) The AQY of M and AKMT samples. (s) Solid-state nuclear magnetic resonance (NMR) spectra of ^{13}C. Reproduced with permission [145]. Copyright 2020, Wiley. (t) Schematic diagram of Ni site structure evolution in the photocatalytic H_2O_2 generation. (u) The time course of H_2O_2 production activities in pure water. (v) Free energy profiles for photocatalytic H_2O_2 evolution reactions. Reproduced with permission [143]. Copyright 2023, Springer.

responding catalytic enhancement mechanisms remain major challenges. Single-atom photocatalysts (SAPs), featuring well-defined single-atom active sites and high atomic utilization, serve as ideal catalytic models to explore the structural evolution of active sites and reaction mechanisms in depth [141,142].

Zhang *et al*. anchored Ni single atoms in a porous carbon nitride matrix (Ni-SAPs/PuCN) with a high loading of 12.5 wt% in Ni-N_3 coordination (Figs. 5t-v) [143]. The catalyst delivered an H_2O_2 production rate of 342.2 μmol L^{-1} h^{-1} in pure water, with an AQY of 10.9 % and an SCC efficiency of 0.82 %. *In-situ* synchrotron X-ray absorption and Raman spectroscopy revealed the dynamic evolution of Ni sites from Ni-N_3 to O_1-Ni-N_2 and finally to HOO-Ni-N_2 during reaction, which reduced the energy barrier for *OOH formation and suppressed O-O bond cleavage. The Ni atoms also optimized the host electronic structure, enhancing charge separation and migration.

In a recent advance, Su *et al*. developed an antimony single-atom catalyst (Sb-SAPC) with Sb^{3+} ($4d^{10}5s^2$) atoms atomically dispersed in a polymeric carbon nitride framework *via* Sb-N bonds [144]. The unique electronic configuration prevented midgap states and facilitated charge separation. Under visible light and without sacrificial agents, the catalyst achieved an AQY of 17.6 % at 420 nm, an SCC efficiency of 0.61 %, and an H_2O_2 production rate 248 times that of the pristine material. The Sb single atoms adsorbed O_2 in an end-on configuration, forming an Sb-OOH intermediate that promotes the $2e^-$ ORR pathway, while simultaneously accelerating the $4e^-$ WOR through hole accumulation on adjacent N atoms. The *in-situ* produced O_2 from WOR was rapidly consumed *via* ORR, creating a synergistic cycle that enhanced overall kinetics.

2.1.3. Co-doping of metal and non-metal element

Heteroatom co-doping can create synergistic effects between metal and non-metal elements, further optimizing the electronic and catalytic properties of g-C_3N_4. Zhang *et al*. constructed a sulfur and potassium co-doped catalyst (AKMT) using thiourea/melamine precursors treated with NaOH/KCl (Figs. 5p-s) [145]. The dopants disrupted the layered structure, generating abundant edge cyano and surface hydroxyl groups. Sulfur was incorporated *via* C-S and N-S bonds, while potassium formed N-K coordination complexes, collectively red-shifting the absorption edge to 500 nm (band gap 2.52 eV) and positively shifting the valence band to 1.89 eV. Under acidic and O_2-saturated conditions, the H_2O_2 yield reached 4.1 mmol/L within 3 h, with a notable AQE of 100 % at 450 nm and 96 % electron selectivity. Transient infrared spectroscopy revealed that sulfur doping extended the lifetime of shallowly trapped electrons and directed deeply trapped electrons toward oxygen reduction. The catalyst also demonstrated potential for practical disinfection applications through *in situ* H_2O_2 generation in tap water, though activity decay in alkaline conditions remains an issue.

In a related study, Wang *et al*. reported a one-pot synthesis of phosphorus-sodium co-doped -C_3N_4 ($Na_{1.2}$-$P_{0.2}$-CN) [146]. Phosphorus substitution formed N-P-N bonds, while sodium intercalation induced cyano group formation and valence band shifts. DFT simulations illustrated that charge density redistribution established a built-in electric field, and transition state calculations confirmed a reduced energy barrier for $^*O_2$ formation. With isopropanol as a sacrificial agent, the H_2O_2 yield reached 3001.64 μmol g^{-1} L^{-1} within 100 min, surpassing the undoped catalyst by 62 times.

2.2. Defect modification

2.2.1. Surface defect engineering

Defects and vacancies, as crucial regulatory units of the electronic structure and surface properties of catalysts, exert a concentration- and type-dependent dual influence on catalytic activity [147]. Typically, precise regulation of defect/vacancy type, concentration, and distribution to balance activity, selectivity, and stability remains a research focus in catalyst engineering. Surface defect engineering is an effective approach to enhance the photocatalytic efficiency of carbon nitride by addressing its inherent limitations, such as restricted visible-light absorption and rapid charge carrier recombination [59,148]. Introducing surface defects can achieve band structure modulation *via* defect-induced energy levels that extend light absorption into the near-infrared region and facilitate carrier separation. Defect sites serve as active centers can optimize reactant adsorption and electron migration, enhancing reaction kinetic.

2.2.1.1. Carbon defects. Wu *et al*. employed an oxalic acid etching-assisted self-assembly method to synthesize flower-like carbon nitride with carbon defects (GCN) (Figs. 6a-d) [149]. Using melamine in DMSO followed by etching and calcination at 550 °C, a porous microstructure with a diameter of 1.2 μm was obtained. The resulting material exhibited a reduced C/N ratio (0.78) and a 1.8-fold stronger EPR signal, confirming enhanced carbon defects that improved O_2 adsorption and promoted the two-electron oxygen reduction pathway, as evidenced by an electron transfer number of 2.50 in RDE tests. The H_2O_2 production rate reached 21.59 mmol L^{-1} g^{-1} h^{-1}, five times that of bulk g-C_3N_4. When applied in a self-Fenton system, it efficiently degraded 2,4-dichlorophenol with a rate constant of 0.070 min^{-1}. Mechanism studies revealed that carbon defects increased carrier separation efficiency, raising the photocurrent density by 300 % and the photoluminescence quenching rate by 60 %. The *in-situ* generated H_2O_2 reacted with Fe^{2+} to produce ·OH, which was confirmed by ESR, and the system showed over 90 % stability in tap water across four cycles, demonstrating practicality for pollutant degradation.

2.2.1.2. Nitrogen defects. Nitrogen defects also play a critical role in modulating the electronic and catalytic properties of g-C_3N_4. Li *et al*. optimized the electronic structure and spin density distribution of carbon nitride (SCN_x) *via* a combined strategy of sulfur doping and edge group modification, enabling efficient photocatalytic H_2O_2 synthesis without sacrificial agents (Figs. 6e-h) [150]. The material exhibited a high surface area (163 m^2/g), a negatively shifted conduction band (-0.92 V), and a narrowed band gap (2.48 eV). Without sacrificial agents, it achieved an H_2O_2 production rate of 416.7 μmol g^{-1} h^{-1} under visible light ($\lambda \geq 420$ nm), 10 times that of pristine g-C_3N_4, with an apparent quantum yield of 31.6 % at 365 nm. *In-situ* IR and theoretical analyses revealed that edge functionalization enhanced O_2 adsorption and reduced the energy barrier of *OOH formation, underscoring the role of spin density localization in promoting reaction kinetics. The H_2O_2 solution (624.8 μmol/L) generated by this catalyst in pure water could efficiently degrade rhodamine B (5 mg/L, >95 % removal within 5 min) and inactivate Escherichia coli, providing a new insight for the design of spin-regulated photocatalysts.

Zeng *et al*. constructed a carbon nitride with multiple active sites (BPMC-Vs) *via* a synergistic strategy of boron-phosphorus dual doping and nitrogen defects, significantly enhancing the efficiency of photocatalytic H_2O_2 synthesis (Figs. 6i-o) [151]. The cooperation of P/B atoms and defects increased local proton coverage and reduced the *OOH energy barrier from 1.121 eV to 0.767 eV. Under visible light and sacrificial agent-free conditions, the catalyst achieved an H_2O_2 production rate of 465 μmol g^{-1} h^{-1} driven by visible light ($\lambda \geq 420$ nm), with a solar-to-chemical conversion efficiency of 0.33 % and a selectivity of 95.2 %. Key contributions included enhanced proton adsorption (*via* P and -C≡N), improved O_2 activation (*via* B and N vacancies), and facili-

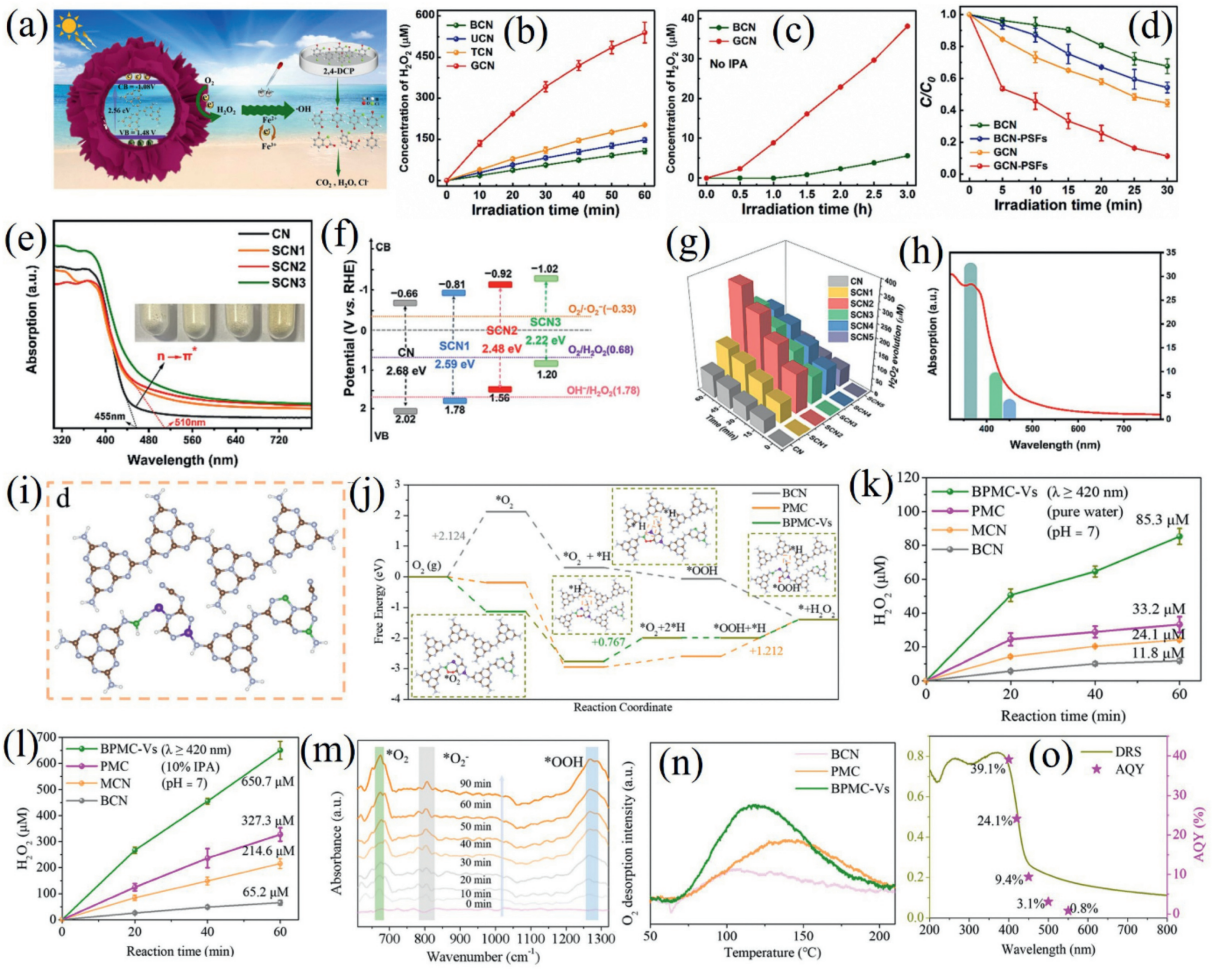


Fig. 6. (a) Possible degradation mechanism. (b) Photocatalytic H_2O_2 generation performance in the presence of IPA. (c) H_2O_2 concertation of BCN and GCN without IPA under visible light irradiation. (d) Photocatalytic decomposition curves. Reproduced with permission [149]. Copyright 2022, Elsevier B.V. (e) UV-visible DRS spectra of CN and SCN_x samples. (f) Estimated band structure. (g) H_2O_2 production under visible light irradiation. (h) AQY for photocatalytic H_2O_2 generation by SCN2. Reproduced with permission [150]. Copyright 2023, Elsevier B.V. (i) Structure model of BPMC-Vs. (j) Free energy results of different samples, time course of H_2O_2 production performance in (k) pure water, and (l) 10 % IPA. (m) *In situ* FT-IR result under light radiation. (n) TPD-O_2 profiles of BCN, PMC, and BPMC-Vs. (o) The wavelength-dependent AQY results. Reproduced with permission [151]. Copyright 2022, American Chemical Society.

tated charge separation, as confirmed by photoelectrochemical and spectroscopy results.

Zhang *et al.* developed a dual-defect catalyst (Nv-C≡N-CN) incorporating both nitrogen vacancies and cyano groups (Figs. 7a-g) [152]. This combination resulted in an electron-rich structure with localized charge distribution, significantly enhancing light absorption, charge separation, and H_2O_2 production, which reached 3093 μmol g^{-1} h^{-1} with an apparent quantum yield of 36.2 % at 400 nm. The nitrogen vacancies facilitated O_2 adsorption and activation, while the cyano groups promoted proton adsorption, collectively improving H_2O_2 formation kinetics.

2.2.2. Defect suppression

Enhancing bulk crystallinity represents another essential route to improve photocatalytic performance by reducing internal defects and suppressing charge recombination. Highly crystalline materials possess ordered atomic arrangements and fewer trap states, thereby promoting the migration of photogenerated carriers to surface reaction sites.

Chen *et al.* proposed an anti-defect engineering strategy to synthesize high-crystallinity carbon nitride (CNT) *via* a molten salt method (Figs. 7h-m) [153]. The material showed well-defined lattice fringes (1.742 nm) and a defect concentration 1.8 times lower than conventional g-C_3N_4. These structural merits led to a carrier separation rate three times higher, a 76 % reduction in radiative recombination, and an extended carrier lifetime of 3.27 ns. The H_2O_2 production rate attained 2.48 mmol g^{-1} h^{-1} with an AQE of 22 % at 400 nm 5.8 times higher than that of traditional carbon nitride. Rotating Disk Electrode (RDE) tests confirmed enhanced selectivity for the two-electron oxygen reduction pathway (electron transfer number n = 1.73), and the conduction band potential shifted negatively to -1.23 V (*vs.* NHE), promoting O_2 reduction kinetics. The *in-situ* generated H_2O_2 further enabled efficient tetracycline degradation *via* a Fenton-like process, achieving 84 % removal within 3 h.

Zhong *et al.* synthesized a potassium-doped highly crystalline g-C_3N_4 photocatalyst (CN-K) using a KI-assisted recrystallization strategy. The as-prepared CN-K exhibited higher interplanar crystallinity, a narrower band gap, and smaller particle size (Figs. 7n-r) [154]. Potassium atoms acted as electron acceptors, shifting the conduction band negatively by 0.35 eV and enhancing the O_2 adsorption energy to -0.93 eV. The CN-K (1:6) sample achieved a photocatalytic H_2O_2 production rate of 7.8 mmol L^{-1} h^{-1}, 220 times higher than that of traditional carbon nitride.

In summary, defect engineering-whether through introducing beneficial surface defects or suppressing bulk defects-offers powerful strategies for enhancing charge behavior and surface reactions, providing a robust foundation for designing highly efficient photocatalysts.

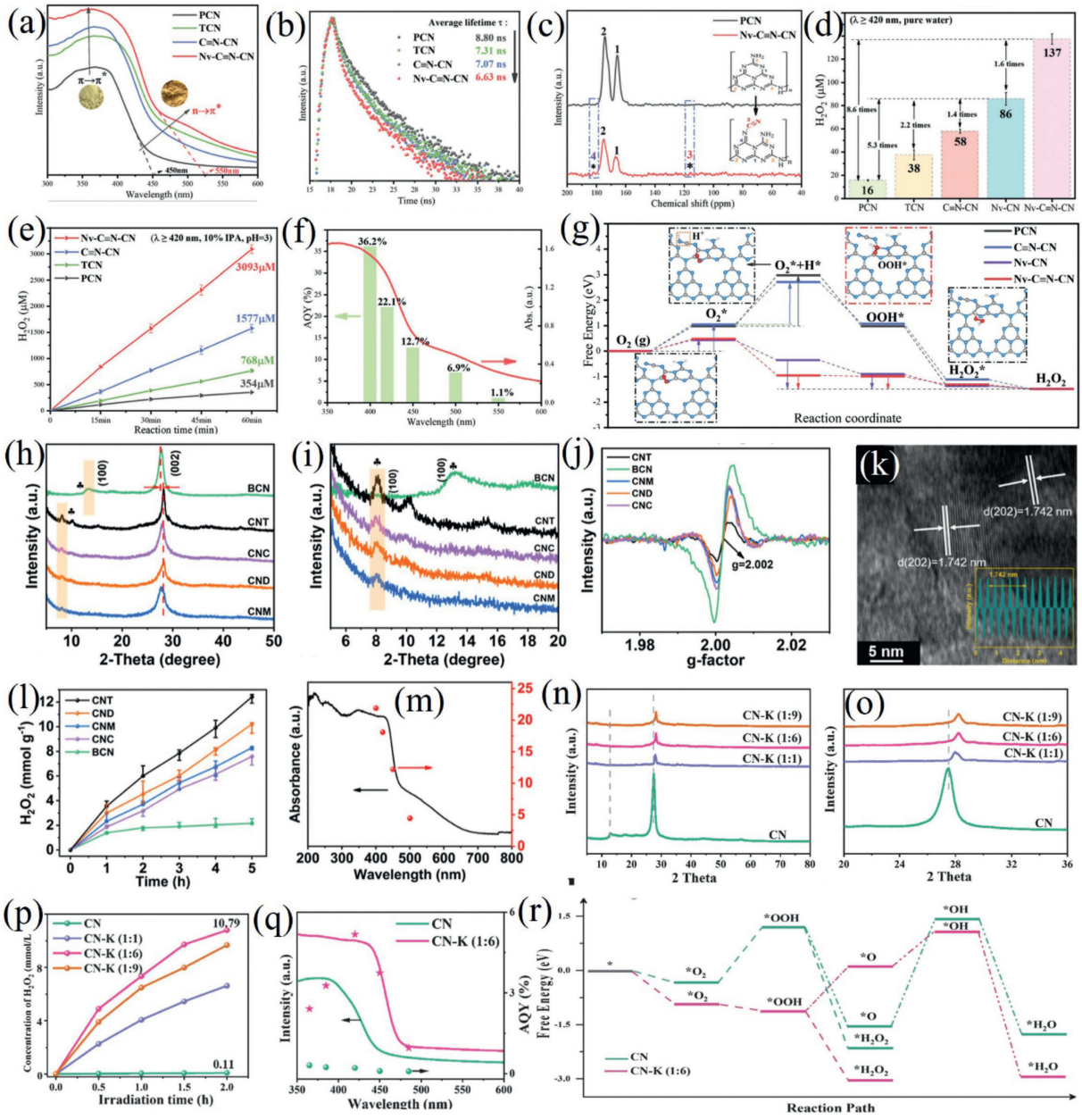


Fig. 7. (a) UV-vis DRS results and (b) time-resolved photoluminescence of the samples. (c) Solid-state ^{13}C MAS NMR spectra. (d) H_2O_2 generation of different samples in pure water. (e) Time course of H_2O_2 production. (f) The wavelength-dependent AQY. (g) Free energy calculation of H_2O_2 evolution reaction. Reproduced with permission [152]. Copyright 2022, Royal Society of Chemistry. (h, i) XRD patterns. (j) ESR g-factor tests. (k) HRTEM image of CNT. (l) Photocatalytic H_2O_2 production performance. (m) Wavelength dependent AQE of CNT. Reproduced with permission [153]. Copyright 2023, American Chemical Society. (n, o) XRD data, (p) photocatalytic H_2O_2 production activities, (q) apparent quantum yield for CN and CN-K. (r) Calculated free energy. Reproduced with permission [154]. Copyright 2024, Chinese Physical Society.

2.3. Junction engineering

Heterojunctions boost catalytic activity through a built-in electric field that separates charges efficiently, while band bending guides charge transfer and blocks recombination [155–160]. New interfacial active sites lower reaction barriers, and tailored electronic structures optimize reactant adsorption, collectively enhancing performance [161–166]. In photocatalytic filed the catalyst composed of two or more semiconductors with tailored band alignments will enhance photocatalytic activity primarily through the formed built-in electric field at the interface, which can significantly suppress non-productive charge recombination [105,167–172]. The combining of a narrow-bandgap semiconductor enables more efficient utilization of solar energy compared to single semiconductors. Finally, the separated electrons and holes retain sufficient reducing and oxidizing capabilities respectively, meeting the energy requirements for target reactions that a single catalyst might fail to achieve. These combined effects collectively boost the overall photocatalytic performance.

2.3.1. Heterojunction

Li *et al.* successfully constructed a $Bi_4Ti_3O_{12}$/g-C_3N_4 (BTOCN) inorganic/organic S-scheme heterojunction photocatalyst *via* an electrospinning-assisted ultrasonic assembly strategy; this composite system formed a tightly contacted S-scheme heterojunction through interface engineering, which significantly optimized carrier kinetic behavior, prolonged carrier lifetime, and notably enhanced the generation of $\cdot O_2^-$ active intermediates and the

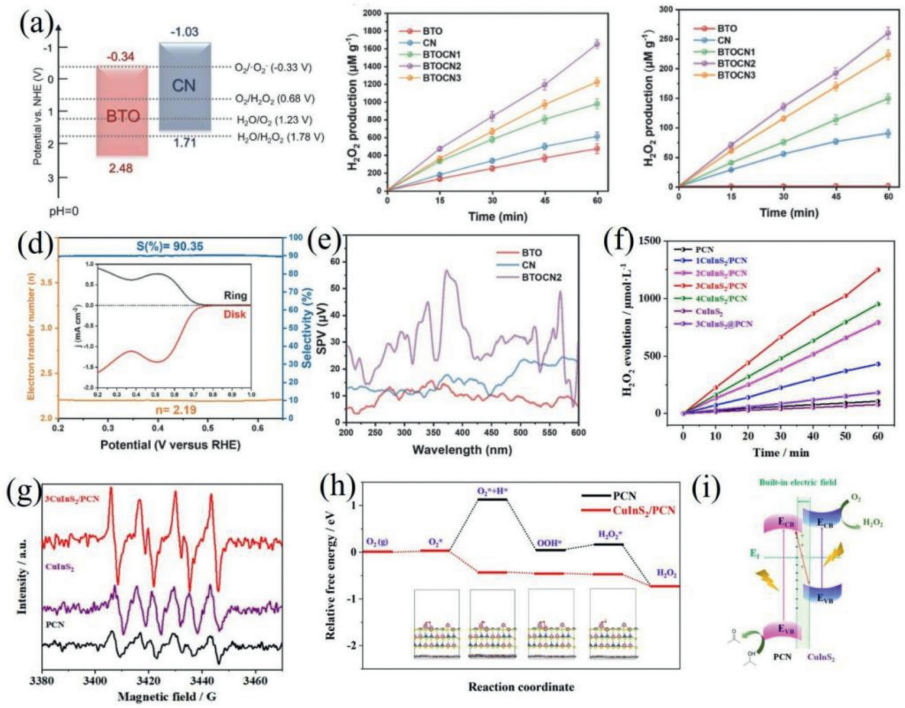


Fig. 8. (a) Band structures of BTO and CN. (b) Photocatalytic H_2O_2 production in 10 vol% methanol aqueous solution and (c) pure water. (d) Calculated electron transfer numbers, H_2O_2 selectivity and RRDE curves of BTOCN2. (e) Surface photovoltage results. Reproduced with permission [173]. Copyright 2024, Chinese Physical Society. (f) Photocatalytic H_2O_2 evolution with different catalysts. (g) ESR signals of DMPO-$\cdot O_2^-$ under visible light irradiation. (h) Free energy profiles. (i) Schematic illustration of S-scheme. Reproduced with permission [174]. Copyright 2023, Elsevier B.V.

two-electron oxygen reduction pathway (Figs. 8a-e) [173]. Under simulated sunlight irradiation, the optimized BTOCN2 sample achieved an H_2O_2 production rate of 260 μmol g^{-1} h^{-1} in pure water, 2.8 times higher than that of single g-C_3N_4, with an apparent quantum yield of 0.36 % at 420 nm, and retained 93 % of its activity after 10 cycles.

In another work, Zhang *et al. in-situ* grew copper indium sulfide ($CuInS_2$) nanosheets on the surface of polymeric carbon nitride (PCN) *via* a low-temperature hydrothermal method, successfully constructing a $CuInS_2$/PCN photocatalyst with an S-scheme heterojunction structure (Figs. 8f-i) [174]. The well-dispersed $CuInS_2$ and tight interfacial contact induced electron transfer from $CuInS_2$ to PCN due to their Fermi level difference, forming a built-in electric field. Under visible light, recombination between PCN electrons and $CuInS_2$ holes preserved electrons with high reducing ability, contributing to an H_2O_2 production rate of 1247.6 μmol g^{-1} h^{-1} in 5 % isopropanol (AQY = 16.0 % at 420 nm), which is 11.6 times and 16.0 times that of individual PCN and $CuInS_2$, respectively.

2.3.2. Homojunction

Homojunctions, composed of the same material with varying phases or morphologies, offer superior lattice matching and lower charge migration barriers than heterojunctions, showing great potential in facilitating charge separation for photocatalytic applications [175–178]. For instance, in a study by Chen *et al.*, a carbon nitride homojunction (homo-CN) was constructed *via* a hydroxyl-induced strategy (Figs. 9a-d) [179]. By *in-situ* growing a hydroxyl-rich carbon nitride (HR-CN) nanolayer on hydroxyl-defective carbon nitride (HD-CN) nanosheets, the synergistic optimization of bulk charge separation and surface reverse reactions was achieved. This design adjusted the band structure by regulating hydroxyl concentration, creating a gradient driving force to facilitate electron-hole separation and extending the light absorption edge. Surface hydroxyl groups provided additional electron-accepting bands, enabling efficient extraction of electrons from the bulk to the surface; meanwhile, they enhanced the adsorption energy of *OOH intermediates and increased the overpotential of the 4-electron oxygen reduction reaction, making the 2e⁻ ORR kinetically more favorable and thus inhibiting H_2O_2 decomposition. Performance tests showed that the H_2O_2 production rate of this homojunction was 4.5 times that of pristine carbon nitride, with an apparent quantum yield of 2.1 % at 500 nm in pure water.

Zhou and his collaborators constructed a novel dual-channel carbon nitride homojunction composite catalyst by incorporating cellulose-derived carbon nanofibers (CF) into the homojunction formed by carbon nitride nanotubes (MCN) and carbon nitride nanosheets (SCN) (Figs. 9e-g) [180]. The MCN/SCN/CF composite exhibited a dual-channel H_2O_2 synthesis mechanism: ORR on the conduction band and WOR on the valence band. The unique structure, coupled with improved light absorption and charge separation, resulted in an H_2O_2 generation rate of 136.9 μmol L^{-1} h^{-1} without sacrificial agents, with an AQY of 4.57 % and solar-to-chemical efficiency of 0.57 %, which was 5 times that of MCN alone.

Zhang's team first fragmented bulk g-C_3N_4 into smaller pieces (CN-NH_4) using a soft template strategy, then subjected them to molten salt treatment for directional splicing, resulting in a homojunction (CN-NH_4-NaK) with multiple ordered-disordered interfaces (Fig. 9h) [181]. The material featured coexisting crystalline and amorphous regions, abundant cyano groups, and a built-in electric field that enhanced charge separation. It achieved an exceptional H_2O_2 production rate of 16675 μmol g^{-1} h^{-1} and over 91 % selectivity across a wide pH range, which is 158 times that of pristine g-C_3N_4. The crystalline domains facilitated H_2O_2 production *via* a two-step single-electron ORR, while the amorphous regions utilized *in-situ* oxygen from water oxidation through a direct two-electron pathway.

In Khan *et al.*'s study, an S-scheme homojunction (B-CN/P-CN) based on boron-doped carbon nitride (B-CN) and phosphorus-doped carbon nitride (P-CN) was constructed for efficient photocatalytic H_2O_2 synthesis (Figs. 9i-l) [182]. The work function

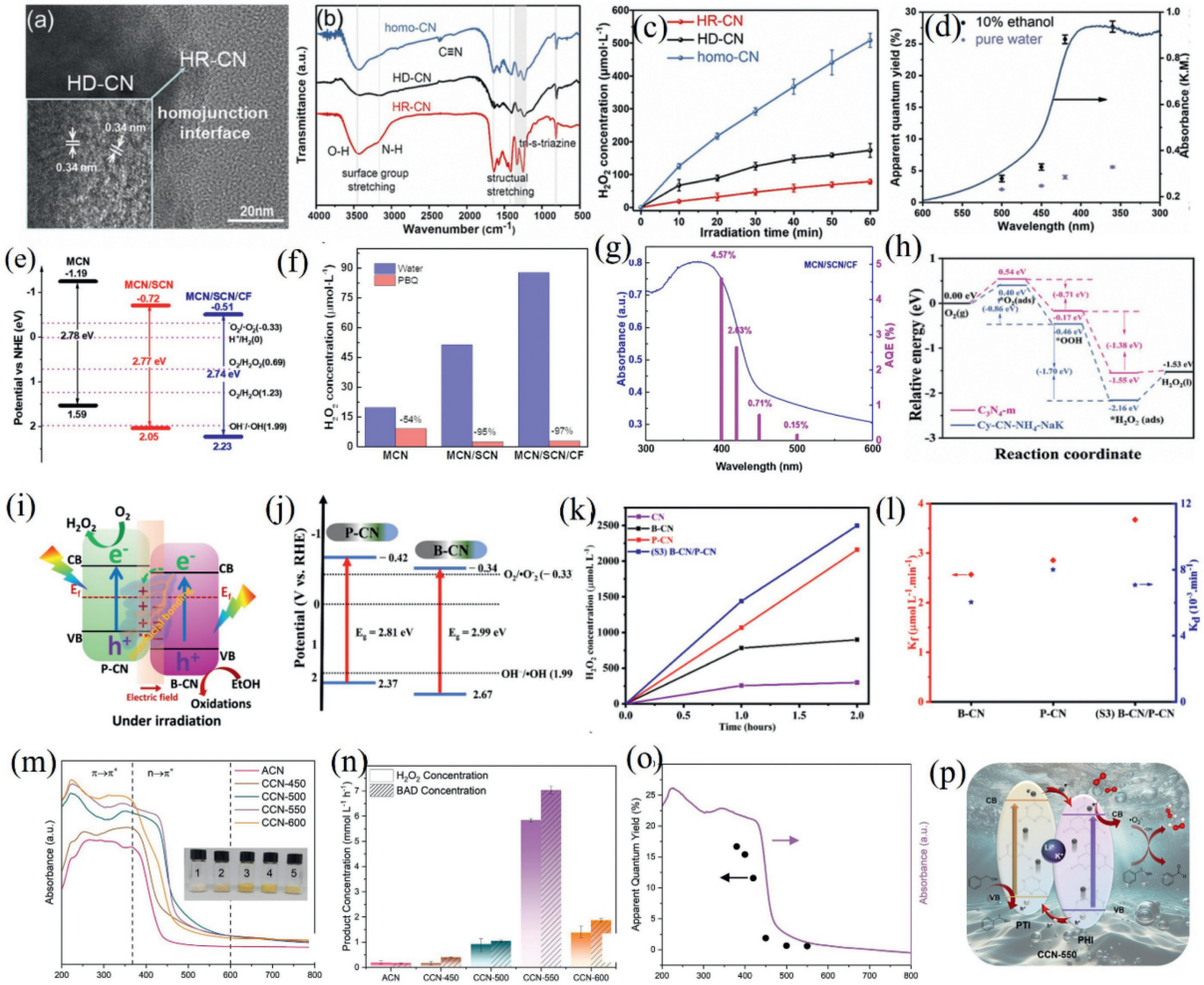


Fig. 9. (a) HRTEM of homo-CN. (b) FT-IR spectroscopy, (c) photocatalytic H_2O_2 of homo-CN, HD-CN and HR-CN. (d) AQY of homo-CN in pure water and 10 % ethanol. Reproduced with permission [179]. Copyright 2023, Elsevier B.V. (e) Energy band structure diagrams. (f) H_2O_2 evolution rate with water or 0.1 mmol/L PBQ. (g) AQE of MCN/SCN/CF. Reproduced with permission [180]. Copyright 2024, Wiley. (h) Free energy diagrams through an indirect two-step single-electron ORR, Reproduced with permission [181]. Copyright 2024, Wiley. (i) The S-scheme charge transfer mechanism. (j) Band structure of the samples. (k) Photocatalytic H_2O_2 generation. (l) k_f and k_d constant of P-CN/B-CN. Reproduced with permission [182]. Copyright 2025, American Chemical Society. (m) UV-vis measurement and photos of the catalysts. (n) Photocatalytic performance of ACN and CCN-X. (o) AQY results. (p) Schematic of the photogenerated charge transmission. Reproduced with permission [184]. Copyright 2025, Elsevier B.V.

difference [183] drove interfacial charge transfer, forming a built-in electric field, while B-P bonds acted as charge migration bridges. The optimal composite showed an H_2O_2 production rate of 2199.5 μmol L^{-1} h^{-1} under 365 nm irradiation, outperforming pristine CN by 2-8 times.

Foo *et al.* synthesized a heptazine/triazine-based crystalline homojunction (CCN-X) *via* one-step ionothermal polymerization (Figs. 9m-p) [184]. KCl and LiCl promoted the formation of cyano/hydroxy groups and triazine units, respectively, while K^+ and Li^+ intercalation enhanced interlayer charge transport. The catalyst simultaneously produced H_2O_2 and benzaldehyde with high yields (5838.91 and 7041.32 μmol L^{-1} h^{-1}, respectively), 100 % selectivity, and an AQY of 11.57 % at 420 nm.

2.3.3. Cocatalyst modification

In photocatalytic H_2O_2 synthesis, the efficient formation of H_2O_2 relies critically on the activation of O_2 or H_2O molecules through well-designed surface sites that lower reaction energy barriers and steer selectivity toward the desired two-electron pathway [185,186]. Beyond intrinsic strategies such as doping and defect engineering, which introduce electron-rich or electron-deficient centers, recent efforts have focused on constructing extrinsic active sites *via* anchored clusters or single atoms [187–189]. These approaches preserve the structural integrity of carbon nitride while improving bulk charge migration and interfacial reactivity through synergistic effects.

For instance, Hou *et al.* constructed a photocatalyst (CoO_x-NvCN) co-modified with surface nitrogen vacancies and CoO_x nanoclusters on polymeric carbon nitride (CN) *via* a two-step method to enhance the performance of $2e^-$ ORR for H_2O_2 production (Figs. 10a-d) [190]. The nitrogen vacancies optimized the electronic structure to facilitate charge separation, while the CoO_x nanoclusters served as high-activity sites that enhanced O_2 adsorption and reduced the energy barrier for *OOH formation. This dual modification resulted in a catalyst capable of producing H_2O_2 at a rate of 244.8 μmol L^{-1} h^{-1} in pure water without sacrificial agents, with an apparent quantum yield (AQY) of 5.73 % at 420 nm and a solar-to-chemical conversion (SCC) efficiency of 0.47 %, ranking among the top-performing carbon nitride-based systems.

In another study, Jing's team designed a boron-doped carbon nitride (BCN) photocatalyst (CoO_x-BCN-FeOOH) modified with dual active sites: Coordinatively unsaturated FeOOH and CoO_x clusters (Figs. 10e-k) [191]. The boron doping optimized the band structure, while the CoO_x clusters promoted water oxidation and extended charge lifetime, and the unsaturated FeOOH clusters facilitated electron acceptance and O_2 activation. The catalyst achieved

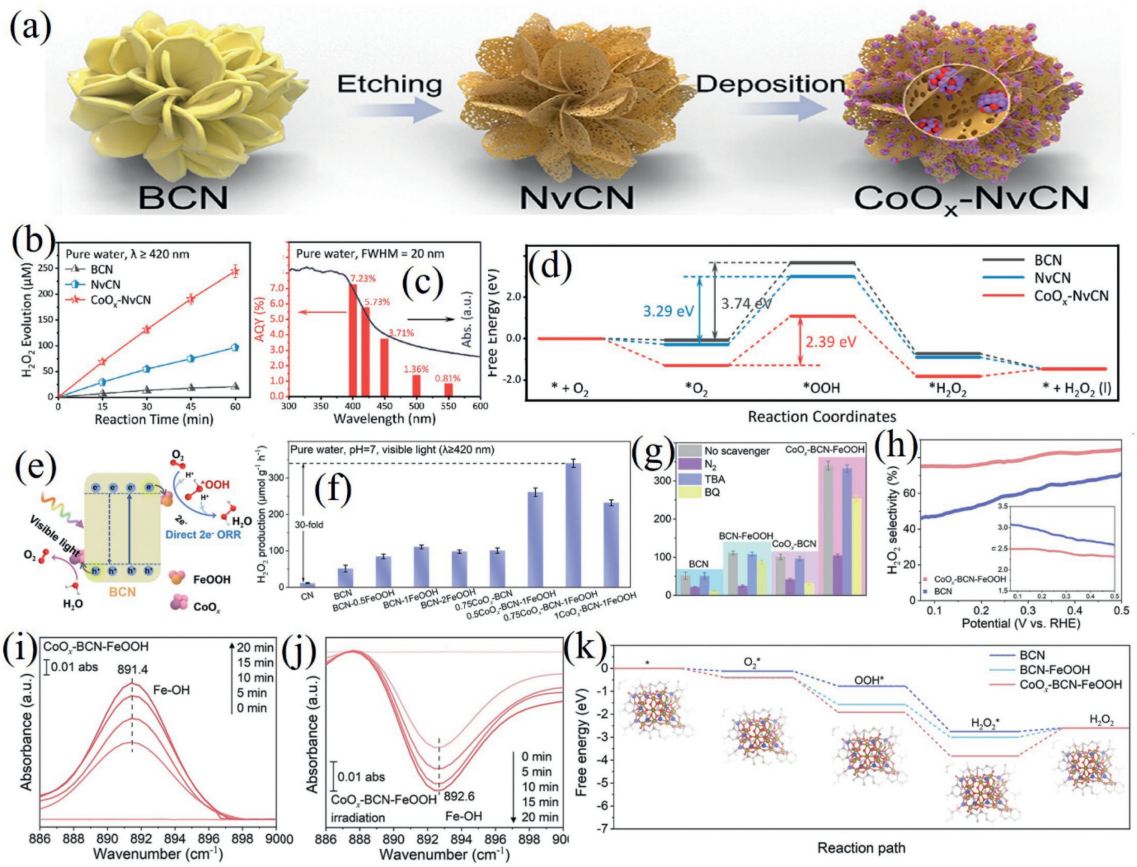


Fig. 10. (a) Schematic illustration of the sample synthesis. (b) Photocatalytic H_2O_2 generation rate. (c) Wavelength-dependent AQY of CoO_x-N_vCN. (d) Free energy diagrams of O_2 reduction reaction. Reproduced with permission [190]. Copyright 2024, American Chemical Society. (e) Schematic of the charge transfer and H_2O_2 generation. (f) Photocatalytic H_2O_2 generation performance. (g) H_2O_2 generation rates under different reaction conditions and the influence of different sacrificial agents. (h) H_2O_2 selectivity characterization. (i) *In situ* DRIFTS of O_2 adsorption over CoO_x-BCN-FeOOH. (j) *In-situ* DRIFTS of CoO_x-BCN-FeOOH during reaction. (k) Free energy diagrams. Reproduced with permission [191]. Copyright 2024, Springer.

an H_2O_2 production rate of 0.34 mmol g^{-1} h^{-1} (30 times that of pristine g-C_3N_4, an SCC efficiency of 0.75% and an AQY of 8.36% at 420 nm). Notably, the FeOOH sites enabled Pauling-type O_2 adsorption, stabilized peroxide intermediates, and increased selectivity for the 2e$^-$ ORR pathway to 85%.

3. Summary and outlook

Due to its distinctive electronic structure, responsiveness to visible light, and metal-free composition, g-C_3N_4 holds significant promise in the photocatalytic synthesis of H_2O_2. Comprehensive investigations into oxygen reduction pathways-including the two-electron 2e$^-$ ORR, $\cdot O_2^-$ mediated pathway, and $^1O_2$-mediated pathway-have elucidated that the formation and stability of critical intermediates such as $\cdot O_2^-$, *OOH, and $^1O_2$ are pivotal determinants of H_2O_2 selectivity. The photocatalytic performance of g-C_3N_4 is collectively influenced by its band structure, surface proton coverage, and the nature of its defects.

Advancements in the mechanistic understanding have facilitated the implementation of various modification strategies, including defect engineering, elemental doping, construction of heterojunctions and homojunctions, and surface-active site modification. These approaches effectively tailor the band structure, enhance light absorption, promote charge carrier separation, optimize oxygen adsorption and activation, stabilize reactive intermediates, suppress H_2O_2 decomposition, improve charge separation efficiency and mass transfer, and reinforce interfacial reaction kinetics and pathway selectivity.

The synergistic integration of these modifications has substantially improved the light-harvesting capability, charge separation efficiency, and surface reaction kinetics of g-C_3N_4, resulting in a marked enhancement of its H_2O_2 production rate under visible light irradiation. Certain systems have demonstrated remarkable stability and applicability across diverse conditions, including pure water, broad pH ranges, and seawater. These advancements have elevated H_2O_2 production rates from trace amounts reported in early studies to the millimole per gram per hour scale, with AQY surpassing 30%, thereby underscoring the potential for transitioning from laboratory-scale research to practical applications.

The band gap of g-C_3N_4, approximately 2.7 eV, constrains its capacity to fully harness visible light, particularly limiting its ability to absorb long-wavelength photons. This limitation impedes further enhancement of solar energy conversion efficiency. Although strategies such as doping, defect engineering, and heterojunction construction have yielded improvements, significant challenges persist due to pronounced electron-hole recombination within the bulk material and at interfaces. Notably, the efficiency of hole utilization in systems devoid of sacrificial agents requires urgent enhancement. Additionally, the competition among multiple reaction pathways-such as 4e$^-$ ORR and H_2O_2 decomposition-remains difficult to suppress entirely. The *in-situ* observation of the dynamic behavior of critical intermediates is also challenging, complicating the rational design of catalysts with high selectivity. Furthermore, most current modification approaches depend on complex precursor designs, high-temperature polymerization processes, and template-assisted synthesis, which collectively hinder

the scalable production of g-C_3N_4 materials with uniform structure and stable performance. Moreover, the majority of investigations have been conducted under controlled laboratory conditions, with limited systematic evaluation of the effects of real-world factors such as impurities in natural water sources, pH variability, and fluctuating light conditions on catalytic performance.

Future progress in g-C_3N_4-based photocatalytic hydrogen peroxide synthesis will necessitate interdisciplinary collaboration and systematic design strategies, aiming for synergistic advancements across three domains: Material development, mechanistic understanding, and device engineering. At the material level, integrating theoretical modeling with *in situ* dynamic characterization techniques is essential to rationally engineer surface structures that exhibit narrowed band gaps, enhanced charge separation, and multisite synergistic effects. Such design will facilitate precise control over oxygen adsorption, proton transfer, and H_2O_2 desorption processes. Regarding light energy utilization, the development of advanced composite systems is imperative to extend light absorption capabilities into the visible and near-infrared spectra. From the perspectives of synthesis and application, it is critical to establish green, low-temperature, and scalable fabrication methods.

In addition, increasing efforts in computational analysis and materials informatics provide useful guidance for the rational design and scalable preparation of g-C_3N_4-based photocatalysts for hydrogen peroxide production. By systematically examining the relationships among precursor chemistry, polymerization conditions, structural modification strategies, and resulting material properties, it becomes possible to identify key compositional and structural features that are beneficial for efficient H_2O_2 generation. This perspective is particularly relevant to g-C_3N_4 systems, where small variations in synthesis parameters, calcination temperature, atmosphere, or post-treatment methods, can lead to pronounced differences in crystallinity, defect distribution, surface chemistry, and electronic structure. A clearer understanding of these structure-property relationships may help guide targeted material optimization and reduce excessive empirical trial-and-error. With further integration of computational analysis and experimental synthesis, g-C_3N_4 photocatalysts with more controllable structures, improved reproducibility, and better scalability are expected to be developed, which will be beneficial for advancing photocatalytic hydrogen peroxide production toward practical applications. Concurrently, efforts should focus on comprehensive validation and long-term stability assessments of photocatalysis-Fenton coupling systems, flow reactors, and performance under actual water body conditions. Ultimately, these endeavors aim to transition this technology from laboratory-scale research to large-scale, sustainable production and environmental remediation applications.

Declaration of competing interest

The authors declare that they have no known competing financial interests or personal relationships that could have appeared to influence the work reported in this paper.

CRediT authorship contribution statement

Zhimin Yuan: Writing – original draft. **Xingling Zhao:** Supervision. **Xianglin Zhu:** Formal analysis. **Kaili Wang:** Data curation. **Ya-Qian Lan:** Conceptualization. **Zaiyong Jiang:** Writing – review & editing.

Acknowledgments

This work was financially supported by the National Natural Science Foundation of China (Nos. 22572148, 22502145, 22402151), the Natural Science Foundation of Shandong Province, China (No. ZR2023MB049).

References

[1] X. Zhang, Y. Wan, Y. Wen, et al., Nat. Catal. 8 (2025) 465–475.
[2] Z. Tian, C. Han, Y. Zhao, et al., Nat. Commun. 12 (2021) 2039.
[3] Z. Yuan, H. Miao, Z. Jiang, et al., Mol. Catal. 577 (2025) 114962.
[4] C. Luo, H. Xi, Y.Q. Feng, et al., Energy Convers. Manage. 267 (2022) 115914.
[5] C. Zhou, Y. Song, Z. Wang, et al., J. Environ. Chem. Eng. 11 (2023) 110138.
[6] H. Jiang, L. Wang, X. Yu, et al., Chem. Eng. J. 466 (2023) 143129.
[7] S. Huo, D. Necas, F. Zhu, et al., Chem. Eng. J. 406 (2021) 127160.
[8] L. Liu, Z. Zhang, J. Wang, et al., Energy 168 (2019) 946–952.
[9] S. Tong, D. Chen, P. Mao, et al., J. Hazard. Mater. 424 (2022) 127622.
[10] X. Li, Y. Wan, F. Deng, et al., Chin. Chem. Lett. 36 (2025) 111418.
[11] Z. Cao, T. Zhou, X. Ma, et al., ACS Sustain. Chem. Eng. 8 (2020) 11007–11015.
[12] J. Liu, M. Zhou, K. Jin, et al., Battery Energy 3 (2024) 20230049.
[13] Y. Shiraishi, Y. Ueda, A. Soramoto, et al., Nat. Commun. 11 (2020) 3386.
[14] T. Gu, J. Ge, A. Li, et al., Int. J. Hydrogen Energy 49 (2024) 764–774.
[15] Z. Liu, X. Liu, L. Tang, et al., Chin. Chem. Lett. 37 (2026) 112024.
[16] C. Wang, X. Xie, F. Qiu, et al., Chin. Chem. Lett. 37 (2026) 111604.
[17] Z. Liu, L. Wang, P. Liu, et al., Food Chem. 357 (2021) 129753.
[18] X. Sun, J. Yang, X. Zeng, et al., Angew. Chem. Int. Ed. 63 (2024) e202414417.
[19] S.M. Chen, L.K. Chen, N. Tian, et al., ACS Catal. 14 (2024) 16664–16672.
[20] K. Wang, M. Wang, Q. Lei, et al., Mol. Catal. 580 (2025) 115121.
[21] Y. Chen, C. Zhen, Y. Chen, et al., Angew. Chem. Int. Ed. 63 (2024) e202407163.
[22] L. Lin, Z. Sun, H. Chen, et al., Acta Phys. Chim. Sin. 40 (2024) 2305019.
[23] N. Bhuvanendran, S. Ravichandran, Q. Xu, et al., Int. J. Hydrogen Energy 47 (2022) 7113–7138.
[24] M. Dan, R. Zhong, S. Hu, et al., Chem. Catal. 2 (2022) 1919–1960.
[25] S. Gao, H. Yang, D. Rao, et al., Chem. Eng. J. 433 (2022) 134460.
[26] W. Li, N. Bhuvanendran, W. Zhang, et al., Int. J. Hydrogen Energy 47 (2022) 24807–24816.
[27] Z. Liu, Y. Bian, G. Dawson, et al., Chin. Chem. Lett. 36 (2025) 111272.
[28] K. Liu, Z. Wang, Y. Xie, et al., Chin. Chem. Lett. (2025), doi:10.1016/j.cclet.2025.111701.
[29] Y. An, T. Cai, W. Jiang, et al., Green Chem. 27 (2025) 10478–10509.
[30] T. Liu, Z. Pan, J.J.M. Vequizo, et al., Nat. Commun. 13 (2022) 1034.
[31] Y. Ding, S. Maitra, S. Halder, et al., Matter 5 (2022) 2119–2167.
[32] W. Wang, L. Wang, L. Sun, et al., Chem. Eng. J. 477 (2023) 146945.
[33] H. Zong, G. Zeng, H. Miao, et al., Appl. Surf. Sci. 649 (2024) 158964.
[34] Z. Yuan, B. Zhang, X. Zhu, et al., Adv. Funct. Mater. 35 (2025) 2503531.
[35] G. Zeng, H. Miao, J. Wu, et al., Chem. Eng. J. 499 (2024) 156367.
[36] H. Miao, G. Zeng, J. Wu, et al., Int. J. Hydrogen Energy 102 (2025) 963–971.
[37] X. Qiu, X. Wang, X. Liu, et al., Chemistry 30 (2024) e202400348.
[38] X. Zhu, H. Zong, C.J.V. Pérez, et al., Angew. Chem. Int. Ed. 62 (2023) e202218694.
[39] S. Shi, H. Zong, Z. Yuan, et al., Inorg. Chem. Front. 12 (2025) 2524–2536.
[40] X. Zhu, E. Zhou, X. Tai, et al., Angew. Chem. Int. Ed. 63 (2025) e202425439.
[41] H. Miao, J. Wu, X. Luo, et al., Inorg. Chem. 64 (2025) 10290–10301.
[42] Y. Xu, M.M. Hassan, S. Ali, et al., J. Agric. Food. Chem. 69 (2021) 1667–1674.
[43] H. Zhang, J. Liu, Y. Zhang, et al., J. Mater. Sci. Technol. 166 (2023) 241–249.
[44] F. Liu, P. Zhou, Y. Hou, et al., Nat. Commun. 14 (2023) 4344.
[45] X. Zhang, X. Zhao, P. Zhu, et al., Nat. Commun. 13 (2022) 2880.
[46] L.J. Li, L.P. Xu, Z.F. Hu, et al., Adv. Funct. Mater. 31 (2021) 2106120.
[47] A.T. Murray, S. Voskian, M. Schreier, et al., Joule 3 (2019) 2942–2954.
[48] Y.Y. Qian, Y.L. Han, X.Y. Zhang, et al., Nat. Commun. 14 (2023) 3083.
[49] Y. Shiraishi, Y. Kofuji, H. Sakamoto, et al., ACS Catal. 5 (2015) 3058–3066.
[50] Y. Shiraishi, S. Kanazawa, Y. Sugano, et al., ACS Catal. 4 (2014) 774–780.
[51] J. Ma, X. Peng, Z. Zhou, et al., Angew. Chem. Int. Ed. 61 (2022) e202210856.
[52] X. Hu, Z. Sun, G. Mei, et al., Adv. Energy Mater. 12 (2022) 2201466.
[53] Q.B. Liao, Q.N. Sun, H.C. Xu, et al., Angew. Chem. Int. Ed. 62 (2023) e202310556.
[54] J. Liu, L. Huang, Y. Li, et al., J. Environ. Chem. Eng. 10 (2022) 106668.
[55] T. Tang, Z. Yin, J. Chen, et al., Chem. Eng. J. 417 (2021) 128058.
[56] X.X. Zhang, Y.G. Xiao, S.S. Cao, et al., J. Cleaner Prod. 352 (2022) 131560.
[57] F. Qiao, W. Liu, J. Yang, et al., Int. J. Hydrogen Energy 53 (2024) 840–847.
[58] Y. Wei, X. Li, Y. Zhang, et al., Renew. Energy 179 (2021) 756–765.
[59] Z. Yuan, X. Zhu, Q. Gao, et al., Molecules 28 (2023) 4057.
[60] X. Pan, F. Kong, M. Xing, Res. Chem. Intermed. 48 (2022) 2837–2855.
[61] X. Gao, L. Cao, Y. Chang, et al., ACS Sustain. Chem. Eng. 11 (2023) 5597–5607.
[62] Z. Du, Z. Zhou, N. Sun, et al., Chin. Chem. Lett. 37 (2026) 111341.
[63] H. Zhang, Q. Su, ACS Omega 10 (2025) 8793–8815.
[64] X. Yan, B. Wang, J. Zhao, et al., Chem. Eng. J. 452 (2023) 139271.
[65] C. Li, H. Che, Y. Yan, et al., Chem. Eng. J. 398 (2020) 125523.
[66] S. Yin, L. Sun, Y. Zhou, et al., Chem. Eng. J. 406 (2021) 126776.
[67] R. Yu, B. Luo, M. Chen, et al., Int. J. Hydrogen Energy 48 (2023) 24285–24294.
[68] C. Zhang, M. Tan, X. Lu, et al., Phys. Chem. Chem. Phys. 25 (2023) 24960–24967.
[69] S. Chen, Y. Qi, T. Hisatomi, et al., Angew. Chem. Int. Ed. 54 (2015) 8498–8501.
[70] C. Li, G. Ding, X. Liu, et al., Chem. Eng. J. 435 (2022) 134740.
[71] J. Rong, G. Zhu, W.R. Osterloh, et al., Chem. Eng. J. 412 (2021) 127556.
[72] Z. Xia, R. Yu, H. Yang, et al., Int. J. Hydrogen Energy 47 (2022) 13340–13350.
[73] C. Li, X. Liu, Y. Yan, et al., Chem. Eng. J. 410 (2021) 128316.
[74] L. Yu, W. Fan, N. He, et al., Int. J. Hydrogen Energy 46 (2021) 17741–17750.

[75] Y.X. He, J.S. Zhao, Y.T. Sham, et al., ACS Sustain. Chem. Eng. 11 (2023) 17552–17563.
[76] H. Guo, S. Wang, X. Chen, et al., Nat. Synth. 4 (2025) 1610–1620.
[77] R. Liu, Y. Chen, H. Yu, et al., Nat. Catal. 7 (2024) 195–206.
[78] X. Liu, X. Yang, X. Ding, et al., Chin. Chem. Lett. 34 (2023) 108148.
[79] X. Pan, J. Ji, N. Zhang, et al., Chin. Chem. Lett. 31 (2020) 1462–1473.
[80] Z. Yuan, X. Zhu, X. Gao, et al., Environ. Sci. Ecotechnol. 20 (2024) 100368.
[81] H. Wang, H. Jiang, P. Huo, et al., J. Environ. Chem. Eng. 10 (2022) 106908.
[82] T. Wang, X. Liu, Q. Men, et al., Renew. Energy 147 (2020) 856–863.
[83] L. Wang, G. Tang, S. Liu, et al., Chem. Eng. J. 428 (2022) 131338.
[84] D. Tsukamoto, A. Shiro, Y. Shiraishi, et al., ACS Catal. 2 (2012) 599–603.
[85] P. Karuppasamy, N.R.N. Nisha, A. Pugazhendhi, et al., J. Environ. Chem. Eng. 9 (2021) 105254.
[86] C. Jin, S. Rao, J. Xie, et al., Chem. Eng. J. 447 (2022) 137369.
[87] W. Wang, G. Zhang, Q. Wang, et al., Chin. Chem. Lett. 35 (2024) 109193.
[88] Y. Qin, H. Li, J. Lu, et al., Chem. Eng. J. 384 (2020) 123275.
[89] J. Tao, M. Wang, X. Zhang, et al., Fuel 338 (2023) 127259.
[90] S. Wang, J. Zhang, B. Li, et al., J. Environ. Chem. Eng. 10 (2022) 107438.
[91] J.Y. Yue, Z.X. Pan, P. Yang, et al., ACS Mater. Lett. 6 (2024) 3932–3940.
[92] Y.Y. Tang, W.M. Wang, J.Q. Ran, et al., Energy Environ. Sci. 17 (2024) 6482–6498.
[93] C.B. Wu, Z.Y. Teng, C. Yang, et al., Adv. Mater. 34 (2022) 2110266.
[94] Z. Lang, X. Wang, S. Jabeen, et al., Adv. Mater. 37 (2025) e2418942.
[95] W. Wang, L. Wang, L. Sun, et al., Chem. Eng. J. 477 (2023) 146945.
[96] S. Wu, H.T. Yu, S. Chen, et al., ACS Catal. 10 (2020) 14380–14389.
[97] L. Wang, Y. Hu, J. Xu, et al., Int. J. Hydrogen Energy 48 (2023) 16987–16999.
[98] C.C. Qin, X.D. Wu, L. Tang, et al., Nat. Commun. 14 (2023) 5238.
[99] R. Justinabraham, A. Durairaj, S. Ramanathan, et al., J. Water Process Eng. 44 (2021) 102422.
[100] N. Su, S. Cheng, P. Zhang, et al., Int. J. Hydrogen Energy 47 (2022) 41010–41020.
[101] J. Ye, D. Yang, J. Dai, et al., Chem. Eng. J. 431 (2022) 133972.
[102] W. Chu, S. Li, H. Zhou, et al., J. Environ. Chem. Eng. 10 (2022) 108623.
[103] Y. Wang, J. Xiong, L. Xin, et al., Chin. Chem. Lett. 36 (2025) 110003.
[104] E. Cui, Y. Lu, Z. Li, et al., Chin. Chem. Lett. 36 (2025) 110288.
[105] Y. Dai, W. Peng, Y. Ji, et al., J. Food Sci. 89 (2024) 8022–8035.
[106] L. Jing, D. Wang, M. He, et al., J. Hazard. Mater. 401 (2021) 123309.
[107] Q. Wang, G. Zhang, W. Xing, et al., Angew. Chem. Int. Ed. 62 (2023) e202307930.
[108] M. Liu, G. Zhang, X. Liang, et al., Angew. Chem. Int. Ed. 62 (2023) e202304694.
[109] M. Xu, X. Zhao, H. Jiang, et al., J. Environ. Chem. Eng. 9 (2021) 106469.
[110] C. Feng, X. Ouyang, Y. Deng, et al., J. Hazard. Mater. 441 (2023) 129845.
[111] W. Chen, Z.-C. He, G.-B. Huang, et al., Chem. Eng. J. 359 (2019) 244–253.
[112] Y. Wang, Y. Tian, L. Yan, et al., J. Phys. Chem. C 122 (2018) 7712–7719.
[113] X.J. Lu, C.Z. Yuan, S. Chen, et al., Langmuir 40 (2024) 11067–11077.
[114] Y. Zhang, J.Y. Qiu, B.C. Zhu, et al., Chem. Eng. J. 444 (2022) 136584.
[115] X.D. Zhang, J.G. Yu, W. Macyk, et al., Adv. Sustain. Syst. 7 (2023) 2200113.
[116] Y. Xue, Y.T. Wang, Z.H. Pan, et al., Angew. Chem. Inter. Ed. 60 (2021) 10469–10480.
[117] Y. Yang, J.J. Liu, M.L. Gu, et al., Appl. Catal. B: Environ. 333 (2023) 122780.
[118] S. Zhao, T. Chen, H. Li, et al., Chem. Eng. J. 472 (2023) 145115.
[119] Z. Sun, W. Wang, Q. Chen, et al., J. Mater. Chem. A 8 (2020) 3160–3167.
[120] J. Lu, Y. Zeng, X. Ma, et al., Polymers 11 (2019) 828.
[121] J. Chen, X. Zhu, Z. Jiang, et al., Inorg. Chem. Front. 9 (2022) 103–110.
[122] H. Che, G. Che, P. Zhou, et al., Chem. Eng. J. 382 (2020) 122870.
[123] P. Sun, Z. Mo, J. Zhang, et al., Chem. Eng. J. 478 (2023) 147337.
[124] J. Wei, Y. Zhang, W. Peng, et al., J. Food Compos. Anal. 144 (2025) 107675.
[125] E. Han, T. Gao, T. Wang, et al., J. Food Compos. Anal. 143 (2025) 107597.
[126] B. Wang, L. Yang, F. Yuan, et al., Electrochim. Acta 439 (2023) 141681.
[127] J. Qi, Q. Li, M. Huang, et al., Colloid. Surf. A 683 (2024) 132998.
[128] J. Wu, C. Li, H. Dong, et al., Renew. Energy 157 (2020) 660–669.
[129] S. Shi, H. Zong, Z. Yuan, et al., Inorg. Chem. Front. 12 (2025) 2524–2536.
[130] J. Yang, Z. Ji, S. Zhang, ACS Appl. Energy Mater. 6 (2023) 3401–3412.
[131] Z. Zhang, P. Luo, L. Gan, et al., Appl. Surf. Sci. 649 (2024) 159118.
[132] Y. Xu, G. Wang, W. Li, et al., Chem. Eng. J. 503 (2025) 158655.
[133] Z. Wei, M. Liu, Z. Zhang, et al., Energy Environ. Sci. 11 (2018) 2581–2589.
[134] G. Yu, K. Gong, C. Xing, et al., Chem. Eng. J. 461 (2023) 142140.
[135] L. Ma, Y. Gao, B. Wei, et al., ACS Catal. 14 (2024) 2775–2786.
[136] H. Zhang, Y. Zhu, Y. Sun, et al., J. Environ. Chem. Eng. 11 (2023) 111122.
[137] Y. Liu, Y. Zheng, W. Zhang, et al., J. Mater. Sci. Technol. 95 (2021) 127–135.
[138] F.N. Habarugira, D. Yao, W. Miao, et al., Chin. Chem. Lett. 35 (2024) 109886.
[139] S. Wu, H. Yu, S. Chen, et al., ACS Catal. 10 (2020) 14380–14389.
[140] L. Chen, C. Chen, Z. Yang, et al., Adv. Funct. Mater. 31 (2021) 2105731.
[141] C. Chu, Q. Zhu, Z. Pan, et al., Proc. Natl. Acad. Sci. U. S. A. 117 (2020) 6376–6382.
[142] Y.B. Li, F.X. Xiao, Chem. Sci. 16 (2025) 2661–2672.
[143] X. Zhang, H. Su, P. Cui, et al., Nat. Commun. 14 (2023) 7115.
[144] Z. Teng, Q. Zhang, H. Yang, et al., Nat. Catal. 4 (2021) 374–384.
[145] P. Zhang, Y. Tong, Y. Liu, et al., Angew. Chem. Int. Ed. 59 (2020) 16209–16217.
[146] Y. Wang, M. Wang, X. Zhang, et al., J. Catal. 440 (2024) 115807.
[147] X. Zhu, J. Yang, X. Zhu, et al., Chem. Eng. J. 422 (2021) 129888.
[148] T. Zhou, Z. Cao, X. Tai, et al., Polymers 14 (2022) 1510.
[149] Y. Wu, J. Chen, H. Che, et al., Appl. Catal. B: Environ. 307 (2022) 121185.
[150] Y. Li, W. Wang, Y. Wang, et al., Chem. Eng. Sci. 282 (2023) 119333.
[151] W. Zeng, Y. Dong, X. Ye, et al., ACS Catal. 15 (2025) 6036–6045.
[152] X. Zhang, P. Ma, C. Wang, et al., Energy Environ. Sci. 15 (2022) 830–842.
[153] J. Chen, W. Gao, Y. Lu, et al., ACS Appl. Nano Mater. 6 (2023) 3927–3935.
[154] W. Zhong, D. Zheng, Y. Ou, et al., Acta Phys. Chim. Sin. 40 (2024) 2406005.
[155] H. Miao, G. Zeng, H. Zong, et al., J. Environ. Chem. Eng. 12 (2024) 113496.
[156] W. Yang, M. Gao, Y. Zhang, et al., J. Food Compos. Anal. 136 (2024) 106738.
[157] S. Meng, D. Liu, Y. Li, et al., J. Agric. Food Chem. 70 (2022) 13583–13591.
[158] H. Wu, S. Yu, Y. Wang, et al., Int. J. Hydrogen Energy 45 (2020) 30142–30152.
[159] S. Vignesh, P. Eniya, M. Srinivasan, et al., J. Environ. Chem. Eng. 9 (2021) 105996.
[160] Y. Cui, J. Zheng, Z. Wang, et al., J. Environ. Chem. Eng. 9 (2021) 106666.
[161] Y. Yang, H. Wang, W. Qin, et al., J. Colloid Interface Sci. 561 (2020) 298–306.
[162] Q. Wu, Q. Gao, L. Sun, et al., Chin. J. Catal. 42 (2021) 482–489.
[163] X. Xu, S. Chen, P. Chen, et al., J. Colloid Interface Sci. 674 (2024) 624–633.
[164] Q. Wu, J. Li, T. Wu, et al., ChemElectroChem 6 (2019) 1996–1999.
[165] Y. Zuo, M. Huang, W. Sheng, et al., Int. J. Hydrogen Energy 47 (2022) 917–927.
[166] X. Zhu, H. Miao, J. Chen, et al., Inorg. Chem. Front. 9 (2022) 2252–2263.
[167] X. Wang, Y. Duan, X. Zhao, et al., Mol. Catal. 573 (2025) 114854.
[168] X. Yu, W. Zhang, L. Ma, et al., Green Chem. 27 (2025) 731–742.
[169] Q. Su, C. Zuo, M. Liu, et al., Molecules 28 (2023) 5576.
[170] S. Ma, L.G. Pan, T. You, et al., J. Agric. Food Chem. 69 (2021) 4874–4882.
[171] X. Du, W. Du, J. Sun, et al., Food Chem. 385 (2022) 132731.
[172] S. Meng, D. Liu, Y. Li, et al., J. Agric. Food. Chem. 70 (2022) 13583–13591.
[173] K. Li, C. Liu, J. Li, et al., Acta Phys. Chim. Sin. 40 (2024) 2403009.
[174] Y. Zhang, X. Chen, Y. Ye, et al., J. Catal. 419 (2023) 9–18.
[175] Z. Yu, X. Yue, J. Fan, et al., ACS Catal. 12 (2022) 6345–6358.
[176] J. Qiu, Y. Wu, S. Jiang, et al., ACS Energy Lett. 8 (2023) 4173–4178.
[177] Y. Lei, W. Si, Y. Wang, et al., ACS Appl. Mater. Interfaces 15 (2023) 6726–6734.
[178] X. Li, Z. Jiang, S. Shi, et al., J. Photoch. Photobio. A 471 (2026) 116709.
[179] Q. Chen, C. Lu, B. Ping, et al., Appl. Catal. B: Environ. 324 (2023) 122216.
[180] J. Zhou, T. Shan, F. Zhang, et al., Adv. Fiber Mater. 6 (2024) 387–400.
[181] F. He, Y. Lu, Y. Wu, et al., Adv. Mater. 36 (2024) e2307490.
[182] S. Khan, M.A. Qaiser, W.A. Qureshi, et al., ACS Appl. Mater. Interfaces 17 (2025) 6249–6259.
[183] H.Z. Zhang, J.J. Liu, Y. Zhang, et al., J. Mater. Sci. Technol. 166 (2023) 241–249.
[184] J.J. Foo, S.F. Ng, S.H. Kok, et al., Chem. Eng. J. 505 (2025) 158992.
[185] Z.M. Zhou, M.H. Sun, Y.B. Zhu, et al., Appl. Catal. B: Environ. 334 (2023) 122862.
[186] T. Yang, Y. Chen, Y.C. Wang, et al., ACS Appl. Mater. Interfaces 15 (2023) 8066–8075.
[187] Q. Ji, X. Yu, L. Chen, et al., Ind. Crop. Prod. 172 (2021) 114064.
[188] J. Liang, H. Li, L. Chen, et al., Ind. Crop. Prod. 193 (2023) 116214.
[189] L. Yu, Z. Mo, X. Zhu, et al., Green Energy Environ. 6 (2021) 538–545.
[190] J. Hou, K. Wang, X. Zhang, et al., ACS Catal. 14 (2024) 10893–10903.
[191] P. Liu, T. Liang, Y. Li, et al., Nat. Commun. 15 (2024) 9224.